The Wind-Induced Wave Growth Rate and the Spectrum of the Gravity–Capillary Waves

YUGUANG LIU AND XIAO-HAI YAN

Center for Remote Sensing, Graduate College of Marine Studies, University of Delaware, Newark, Delaware

(Manuscript received 1 December 1994, in final form 29 June 1995)

ABSTRACT

A form of the spectrum of gravity–capillary waves is suggested, based on a balance of the wind input, the spectral flux divergence, the viscous dissipation, and the modulation from the wave–drift interaction. The spectrum in the alongwind direction is expressed as

$$\Phi(k, 0) = mk^{-4}\left(\frac{u_* - \delta}{c}\right)^2\left[1 - \exp\left(-\frac{c^2}{\alpha m_0^2}\right)\right],$$

where k is the wavenumber, m and α are constants, u_* is the wind friction velocity, δ is the threshold wind friction velocity, c is the short-wave phase velocity, and m_0 is the zeroth moment of nondirectional frequency spectrum of long-wave orbital velocity. For shorter capillary waves, the addition of dissipation due to the eddy viscosity is needed.

A kinematic wave breaking criterion is applied in the calculation of the short-wave dissipation. It is found that this short-wave dissipation, due to wave–drift interactions, has the effect of suppressing the spectrum at higher wind speeds and yields a good agreement with the measurements of both the wave spectrum and the wave directional spreading rate. It is also found that the fluctuation of average wind stress and dissipations due to molecular viscosity and eddy viscosity have an important influence on the wave growth rate and the gravity–capillary wave spectrum. The molecular viscosity plays a significant role at lower wind conditions; the eddy-viscous dissipation dominates at higher wavenumbers. The threshold wind friction velocity is determined by a balance between the wind input with fluctuation and the molecular-viscous dissipation. Its value in the fully developed stage is different from that when the wind starts to blow. The fluctuation of the average wind stress arising from the wind turbulence has been considered in the calculation of the short-wave growth rate, and its effect of increasing short-wave growth rate at low winds has been shown.

ERS-1 scatterometer models and radar backscatter measurements in the open ocean are used to confirm the proposed spectrum model, especially the directional spreading function. The results show a good agreement between our model and the field measurements.

1. Introduction

Understanding the scatterometer signal requires us to focus our attention on ocean surface microscale features. Radar backscatter is proportional to the "roughness" of the ocean surface; the roughness is measured with the directional spectrum of the short waves in the range relative to Bragg resonance. The long background waves influence both the spectrum of the short water surface waves and the resulting radar backscatter signal.

Water wave spectra in the equilibrium range have been investigated by Toba (1973), Kitaigorodskii (1983), Phillips (1985, 1988), Durden and Vesecky (1985), Plant (1986), Donelan and Pierson (1987), Banner (1989, 1990), Shemdin et al. (1988), Jähne and Riemer (1990), Klinke and Jähne (1992), Hwang et al. (1993), Apel (1994), and Zhao (1994).

The empirical models proposed by Toba (1973), Durden and Vesecky (1985), and Banner (1989) are based on their measurements with the aid of the dimensional analysis. The emphasis in these studies is how the short waves depend on the wind friction velocity and the wavenumber. A semi-empirical and semiphysical model suggested by Apel (1994) is based on the measurements of Klinke and Jähne (1992) and his understanding of the relevant physical processes. The physical models proposed by Phillips (1985), Plant (1986), and Donelan and Pierson (1987) are based on their recognition of the wind-induced wave growth rate and the relevant physical processes. The wind-induced wave growth rate has been investigated by, among others, Miles (1959), Plant (1982), Donelan and Pierson (1987), Larson and Wright (1975),

Corresponding author address: Dr. Xiao-Hai Yan, Center for Remote Sensing, Graduate School of Marine Studies, University of Delaware, Newark, DE 19716-3501.
E-mail: xiao.yan@mvs.udel.edu

Townsend (1972), Stewart (1974), Snyder et al. (1981), and Hsiao and Shemin (1983).

Plant's (1982) model fits the measurements well in the range of short gravity waves, but it does not work in the range of capillary waves. We found that his model, with the addition of viscous dissipations and fluctuation of wind stress, can work very well in the range of capillary waves. It is necessary to distinguish the two types of viscosity. The molecular-viscous dissipation plays a role at lower winds. The eddy-viscous dissipation dominates at higher wavenumbers.

A difficulty in wind–wave relations is how to treat the fluctuations of wind stress on the moving, random water surface, which is under the influence of both the wind and the long water surface waves. The total surface stress is the sum of directly induced variations by water waves and the random contributions arising from atmospheric turbulence. The variations and fluctuations of wind stress have been investigated by Reynolds and Hussain (1972), Chang et al. (1971), and Takeuchi et al. (1977). Takeuchi et al. (1977) found that the distributions of u' and w' are approximately Gaussian in the range of $u' \pm 3\sigma_u$ and $w' \pm 3\sigma_w$ (σ is the root of variance). Here $-\rho_a\overline{u'w'}$ was used to represent the turbulence Reynolds stress. Stress fluctuation influences wave growth. For an extreme example, Keller et al. (1985) found a significant increase in the radar return with increasing atmospheric instability. In this paper, the variation in wind stress on a larger scale is termed as the "fluctuation" of the wind stress averaged on a finer scale. It has the effect of increasing the short-wave growth rate. This effect on the short-wave growth is found in the comparison of Plant's (1982) model with measurements by Larson and Wright (1975).

Small-scale waves may be modulated by larger-scale features such as large-scale gravity waves, internal waves, tidal currents, and bottom topography (Komen and Oost 1989). A kinematical wave breaking criterion (Banner and Phillips 1974) is that kinematic instability occurs when fluid particles at the free surface are moving forward with a velocity greater than the wave phase velocity. A further question is How does one apply this criterion to calculate the short-wave dissipation? Smith (1986, 1990) combined and extended two previous arguments by Longuet-Higgins (1969) and Phillips and Banner (1974) to estimate dissipation. We use a series of approximations to simplify our results in order to apply this criterion to the calculation of spectral action losses.

Based on our understanding of the relevant physical processes, the wind-induced wave growth rate and the spectral balance of the gravity–capillary waves are investigated in the following sections.

2. Wind-induced wave growth rate

From a survey of field and laboratory experiments, Plant (1982) suggests that

$$\frac{\beta_0}{\omega} = (0.04 \pm 0.02)\left(\frac{u_*}{c}\right)^2, \tag{1}$$

for the wind-induced wave growth rate β_0 over the frequency range from $g/(2\pi U_{10})$ to 20 Hz. Here U_{10} is the wind speed at 10 m, ω is the angular frequency, u_* is the wind friction velocity, and c is the water wave phase velocity; β_0 is used to represent the growth rate without consideration of dissipation. The above relation is in agreement with the theory of Miles (1959), but it fails at small values of u_*/c. Miles's theory (Miles 1959; Plant 1982) is expressed as

$$\beta = \frac{\rho_a \epsilon u_*^2 \omega}{\kappa^2 \rho_w c^2} - 4\nu\omega^2 c^2, \tag{2}$$

where κ is the von Kármán constant, ϵ is a function of u_*/c, and ν is the kinematic molecular viscosity; ρ_a and ρ_w are air and water densities.

Combining Eqs. (1) and (2), we have

$$\frac{\beta}{\omega} = 0.04\left(\frac{u_*}{c}\right)^2 - \frac{4\nu k^2}{\omega}, \tag{3}$$

where k is the water wavenumber.

Equation (3) was found to be incorrect when it was compared with measurements over the range of capillary waves. For capillary waves, the molecular viscosity, the eddy viscosity, the modulation from the wind drift, and the fluctuation of the average wind stress play different but important roles. It is not sufficient to consider only the molecular viscosity.

The theoretical equation for the short-wave dissipation rate due to the molecular viscosity is (Lamb 1932)

$$\frac{\beta_m}{\omega} = -\frac{4\nu k^2}{\omega}. \tag{4}$$

This is the second term on the right side in (3). Without considering the random fluctuations of average wind stress, the threshold wind friction velocity u_0 can be derived from Eq. (3) as

$$u_0 = \left[\frac{4\nu kc}{0.04}\right]^{1/2}. \tag{5}$$

This threshold wind friction velocity means that there is no wave growth if the wind friction velocity is less than u_0.

The actual wind stress is random because the wind is a set of many wind gusts. The ensemble average wind stress can be expressed by

$$\tau_0 = \rho_a u_*^2. \tag{6}$$

Similarly, we define a relation between a random variable τ_i (which is termed as "the local average wind stress" and is obtained by averaging in a finer scale of

time or space) and another random variable u_i (which is termed as "the local wind friction velocity"):

$$\tau_i = \rho_a u_i^2, \tag{7}$$

where u_i, the local wind friction velocity, is a random variable, with an assumption of Gaussian distribution

$$f(u_i) = \frac{1}{\sqrt{2\pi}\sigma} \exp\left[-\frac{(u_i - u_*)^2}{2\sigma^2}\right], \tag{8}$$

where the wind friction velocity u_* is its mean value and σ is its variance.

The ensemble average wind stress can be measured by (Large and Pond 1981; Wen and Yu 1984)

$$\tau_0 = -\rho_a \overline{u'w'}, \tag{9}$$

where $-\rho_a \overline{u'w'}$ is the vertical momentum flux, and u' and w' are the turbulence velocity components in x and z directions, respectively. A local average wind stress τ_i, similar to (7), can be expressed by

$$\tau_i = -\rho_a u'w'. \tag{10}$$

Actually, u' and w' are measured in an interval of several seconds, which belongs to a finer scale of time. So, u' and w' can be termed as "the local turbulence velocity components." Combining (7) and (10), we have

$$u_i^2 = -u'w'. \tag{11}$$

The distribution of u' and w' was found to be approximately Gaussian (Takeuchi et al. 1977). Therefore, the local wind friction velocity u_i can be assumed to obey a Gaussian distribution also.

The above expressions may be out of our traditional understanding of the average wind stress and the corresponding wind friction velocity. Both time and space scales are very small for the capillary waves. The wind stress can be averaged on various scales. We understand that the average wind stress, which can be used to calculate the amount of work done, should be obtained by averaging stress variations on a relatively small time or space scale. Therefore, the wind stress and the friction velocity, which are used to calculate the wave growth rate, should be τ_i and u_i, rather than τ_0 and u_*. Evidence for this understanding is from P. A. Hwang (1994, personal communication): The field data from the High Resolution Experiment (HiRes) show that the energy density of the gravity–capillary waves, generated by wind with the friction velocity $u_* = 4.7$ cm s^{-1}, is about five times the energy density, with $u_* = 4.4$ cm s^{-1}. Obviously, the differences in the energy density are caused by different variances of the wind stress fluctuations rather than the ensemble averages of the wind stress. This new understanding will help us to obtain a good agreement between theory and measurements. Considering the fluctuation of the average wind stress, the wave growth rate can be expressed as

$$\frac{\beta}{\omega} = \int_{u_0}^{\infty} \left[0.04\left(\frac{u_i}{c}\right)^2 - \frac{4\nu k^2}{\omega}\right] f(u_i)\,du_i$$

$$= \int_{u_0}^{\infty} 0.04 \frac{(u_i^2 - u_0^2)}{c^2} f(u_i)\,du_i, \tag{12}$$

where the threshold wind friction velocity u_0 is given by (5) and the probability density $f(u_i)$ is given by (8).

Following the traditional method (Wen and Yu 1984), the dissipation rate due to the eddy viscosity is given by simulating the case of the molecular viscosity:

$$\frac{\beta_e}{\omega} = -\frac{4\nu_e k^2}{\omega}, \tag{13}$$

where ν_e is the eddy viscosity coefficient. Considering both molecular and eddy viscosities, the threshold friction velocity u_0 is given as

$$u_0 = \left[\frac{4(\nu + \nu_e)kc}{0.04}\right]^{1/2}. \tag{14}$$

When wind initially starts to blow, the water surface drifts are generated immediately. The modulation due to the drifts will depress the wave growth rate. The detail of the modulation will be introduced in section 3. Considering the three dissipation processes, the wind-induced wave growth rate is expressed as

$$\frac{\beta}{\omega} = \int_{u_0}^{\infty} 0.04 \frac{(u_i^2 - u_0^2)}{c^2} f(u_i)\,du_i$$

$$\times [1 - \exp(-c^2/\alpha u_*^2)], \tag{15}$$

where the threshold wind friction velocity u_0 is given by (14), the distribution density $f(u_i)$ is given by (8), the factor within the last pair of brackets on the right side represents the modulation from drifting currents, and α is a parameter related to fetch.

A comparison of Eq. (15) with the measurements by Larson and Wright (1975) is shown in Fig. 1. Plant's model fits the measurements very well in the range of short gravity waves, except at small values of u_*/c (Plant 1982, see his Fig. 2). Figure 1 shows that his model, with an addition of the molecular–viscous dissipation and the fluctuation of wind stress (which is represented by shaded area), can fit the measurements very well at small values of u_*/c. Figure 1 also shows that the dissipation rate due to molecular viscosity is obvious at low wind friction velocities, the dissipation rate due to eddy viscosity is significant at very high wavenumbers, and the modulation from wind drift takes place at high wind friction velocities.

Equation (15) includes an integral, which complicates the problem. In order to simplify the equation, we use (16) or (17), which are approximately equivalent

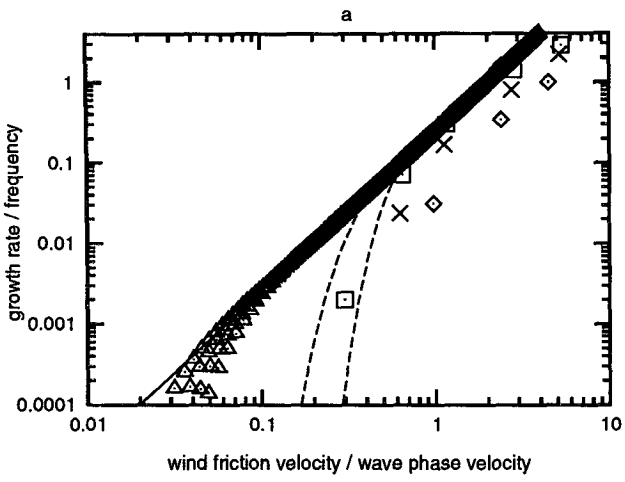

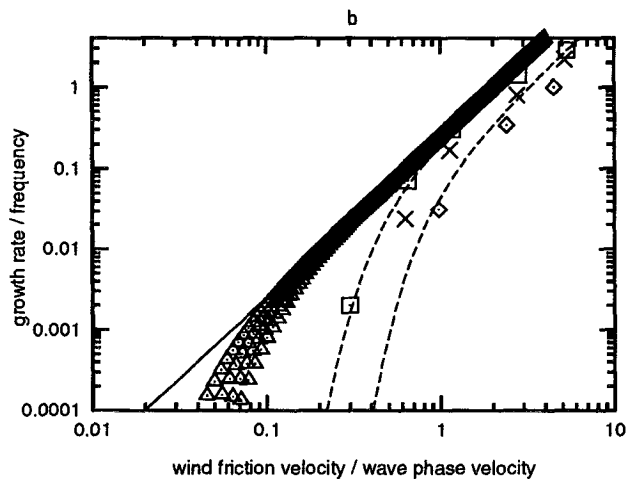

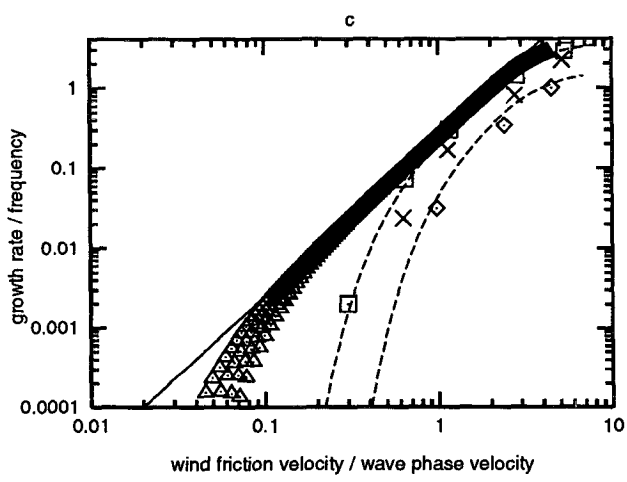

mathematically to (15), to substitute for (15). These two equations are

$$\frac{\beta}{\omega} = 0.04\left(\frac{u_*}{c}\right)^2 \exp\left[-\frac{4(\nu + \nu_e)k^2/\omega}{0.04\left(\frac{u_*}{c}\right)^2/\gamma}\right] \times [1 - \exp(-c^2/\alpha u_*^2)] \quad (16)$$

and

$$\frac{\beta}{\omega} = 0.04x^2 \exp\left[-\frac{4\nu_e k^2/\omega}{0.04x^2/\gamma}\right][1 - e^{-1/\alpha x^2}], \quad (17)$$

with

$$x = (u_* - \delta)/c,$$

$$\delta = 0.8 \text{ (cm s}^{-1}\text{)} + 1.1 \text{ (cm}^2 \text{ s}^{-1} \text{ rad}^{-1}\text{)}k,$$

$$\gamma = 0.12\omega^{1/2},$$

where $0.04(u_*/c)^2$ represents the wind input, $0.04(u_* - \delta)/c^2$ represents the wind input reduced by molecular-viscous dissipation,

$$\exp\left[-\frac{4\nu k^2/\omega}{0.04\left(\frac{u_*}{c}\right)^2/\gamma}\right]$$

represents the influence from molecular viscosity, and

$$\exp\left[-\frac{4\nu_e k^2/\omega}{0.04\left(\frac{u_*}{c}\right)^2/\gamma}\right]$$

represents the influence from eddy viscosity. The factor within brackets on the right side in (16) and (17) rep-

FIG. 1. Wind-induced growth rate normalized by wave frequency (β/f) versus friction velocity per unit phase velocity (u_*/c). Solid line indicates growth rates inferred from Plant (1982). Shaded area (filled by many triangles) indicates growth rates inferred from (15) when k is from 20 rad m^{-1} to 50 rad m^{-1}. Left and right dashed lines indicate growth rates inferred from (15) when k = 340 rad m^{-1} and k = 867 rad m^{-1}, respectively. Squares, crosses, and rhombuses indicate the measurements from Larson and Wright (1975) for k = 340 rad m^{-1}, 501 rad m^{-1}, and 867 rad m^{-1}, respectively. The data were from their Figs. 8 and 9. Three different cases of Eq. (15) are shown in (a), (b), and (c), respectively. (a) The growth rates (dashed lines and shaded area) were inferred from Eq. (15) with calculation of only wind input and molecular–viscous dissipation; (b) with calculation of wind input, dissipations due to molecular viscosity and eddy viscosity; (c) with calculation of wind input and total three dissipations due to molecular viscosity, eddy viscosity, and modulation from wind drift. The probability density $f(u_i)$ in (15) is given by (8). The relevant parameters are the variance in (8) $\sigma = 0.9u_*^{1/2}$, the parameter α in (15) is valued as 0.06, the molecular viscosity in (14) $\nu = 0.011$ cm^2 s^{-1}, the eddy viscosity in (14) $\nu_e = 8 \times 10^{-5}\omega(u_*/c)^2$.

resents the modulation from the wind-induced drift, α is a parameter related to fetch, δ is the threshold friction velocity determined by a balance between the wind input with fluctuation and the molecular viscosity, the parameter γ is a dimensionless coefficient that controls the extent of dissipation and is related to the variance of the local wind friction velocities. In order to emphasize the physical meaning, and for ease of understanding, the exponential functions in (16), (17) and the following equations in this paper are not reduced to their simplest forms.

Equation (1) represents the growth rate without the consideration of the three dissipations. It is approximately correct in the range of gravity waves, because the influence from these three dissipations in this range is small. In the range of shorter waves, the three dissipations cannot be neglected. The factors of these dissipations are defined as

$$f_m = \exp\left[-\frac{4\nu k^2/\omega}{0.04(u_*/c)^2}\gamma\right], \quad (18)$$

or

$$f_m = \left(1 - \frac{\delta}{u_*}\right)^2, \quad (19)$$

and

$$f_e = \exp\left[-\frac{4\nu_e k^2/\omega}{0.04(u_*/c)^2}\gamma\right], \quad (20)$$

$$f_b = (1 - e^{c/\alpha u_*^2}), \quad (21)$$

or

$$f_b = (1 - e^{1/\alpha x^2}), \quad (22)$$

where f_m is the factor of molecular viscous dissipation, f_e is the factor of eddy viscous dissipation, and f_b is the factor of dissipation due to wave–drift (background drift) interactions. In physics, a negative exponential function based on the natural number (e) has often been used successfully to describe dissipation. The negative exponents in (18) and (20) consist of three parts: an energy dissipation rate, an energy input rate, and a coefficient. Here $4\nu k^2/\omega$ in (18) and $4\nu_e k^2/\omega$ in (20) are the energy dissipation rates, $0.04(u_*/c)^2$ in (18) and (20) is the energy input rate, $\gamma(\omega)$ in (18) and (20) is the dimensionless coefficient, f_m in (19) is another form of the dissipation factor; f_b in (21) and (22) will be introduced in section 3.

We use β_0/ω in (1) to represent the growth rate without dissipation. Then the data calculated from $(\beta_0/\omega)f_m$ are very close to the dashed lines in Fig. 1a, the data calculated from $(\beta_0/\omega)f_m f_e$ are very close to the dashed lines in Fig. 1b, and the data calculated from $(\beta_0/\omega)f_m f_e f_b$ are very close to the dashed lines in Fig. 1c. The product of the growth rate with the three dissipation factors $(\beta_0/\omega)f_m f_e f_b$ is equal to the right side of (16) or (17). The dashed lines in Fig. 1 are calculated from (15). Therefore, (16) and (17) are approximately equivalent mathematically to (15).

A comparison of Eq. (17) with the measurements of Larson and Wright (1975) is shown in Fig. 2a. Figure 2a gives almost the same dashed lines as those in Fig. 1c. It means that Eq. (17) can be used to replace Eq. (15). To determine the relative errors, Eq. (17) is rewritten as

$$\frac{\beta}{f}\frac{1}{(f_m f_e f_b)} = 2\pi(0.04 \pm 0.02)\left(\frac{u_*}{c}\right)^2, \quad (23)$$

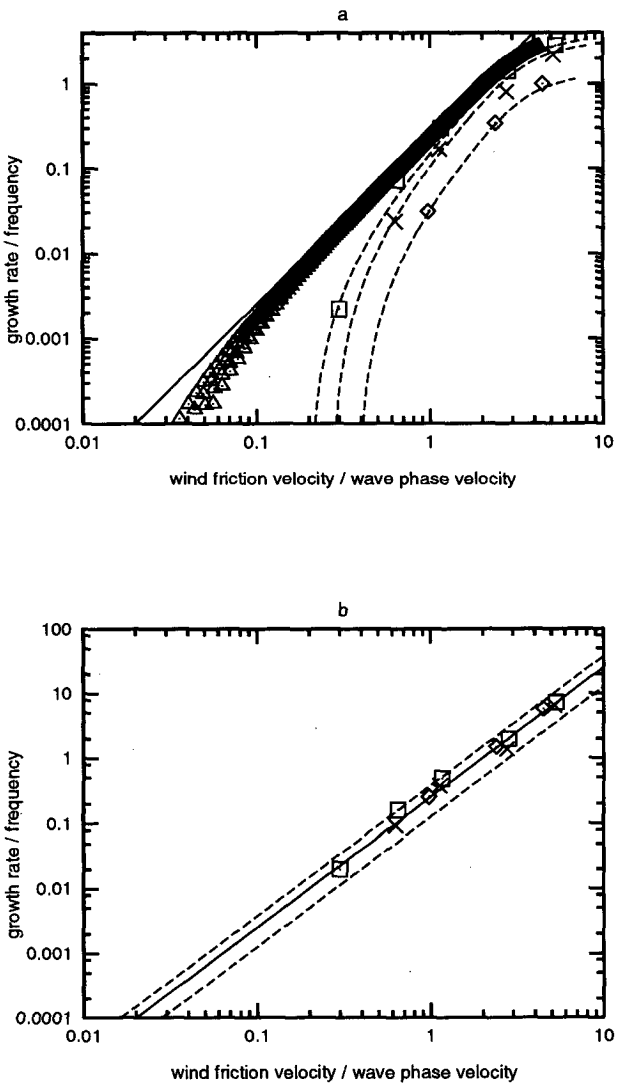

FIG. 2. (a) Similar to Fig. 1c except that the proposed growth rates are calculated from Eq. (17) rather than (15). The three dashed lines from the left to the right are for k = 340, 501, and 867 rad m^{-1}, respectively. (b) Similar to Fig. 1c except that the data measured by Larson and Wright (1975) are added the losses due to three dissipations by using the left of Eq. (23).

where the right side is the growth rate without dissipation by Plant (1982), and $2\pi \times 0.02(u_*/c)^2$ is the standard deviation derived from his data, which means a relative error of 50/100. Plant's growth rate is shown in Fig. 2b as a solid line. The growth rate plus a standard deviation is shown as the upper dashed line, and the growth rate minus a standard deviation is shown as the lower dashed line. The data of Larson and Wright (1975) represent the dissipated growth rate. The left side of (23), in which these data were substituted into β/f, represents the growth rate without dissipation. The data of their measurements plus losses due to three dissipations are shown in Fig. 2b as discrete symbols. Figure 2b shows that these data are within the limits of the above standard deviations. The differences between the measurements and the proposed growth rate are smaller than the standard deviation derived from Plant's data.

The wind-induced growth rate proposed here by using u_* is based on Miles's theory (Miles 1957, 1959) of wind wave generation and development and energy balance among the wind input and the three dissipations. The growth rate proposed by Donelan and Pierson (1987) is based on Phillips's resonance theory of wind wave generation and is expressed by the wind velocity at a height of half-wavelength over water surface. Wind wave generation is a very complicated topic that has been discussed for a few decades. We think that science would benefit from the existence of two theories. Some of the theoretical studies on the wind-induced wave growth rate refer to the theory of wind wave generation. The growth rates measured at very low wind speeds were significantly larger than those predicted by all treatments of the Miles's theory (Valenzuela 1976; Kawai et al. 1977; Van Gastel et al. 1985). Because of this, Kahma and Donelan (1988) gave their explanation by using Phillips resonance theory. Their conclusion is that Phillips resonance theory may be more reasonable than Miles's theory. Our study reveals that the growth rates measured at very low wind speeds are in agreement with those predicted by Miles's theory when the statistics of varying wind fields is included. Therefore, the final choice between the two theories is still unavailable.

3. Short-wave dissipation due to wave–drift interactions

In a very strong wind-generated situation with steep dominant waves, the average spectral density at wavenumbers in the equilibrium range will be suppressed by additional significant local spectral action losses near the dominant wave crests. To find the overall spectral density, one would have to examine the influence from the interactions among the wind drift, the short waves, and the dominant background waves.

With the assumption that the surface wind-drift layer is established by viscous action over a timescale much greater than the time it takes a fluid element to move from crest to trough, a kinematic breaking criterion was derived by Banner and Phillips (1974): kinematic instability occurs when fluid particles at the free surface are moving forward with a speed greater than the wave speed. Laboratory observations by using flow visualization techniques also found that the breaking of wind-generated waves occurs due to kinematical instability. Further evidence that breaking is the result of kinematic instability is given by theory (Thornton 1977).

As given by Phillips and Banner (1974), the maximum amplitude that the short waves can have when they are at the point of incipient breaking at the long-wave crest is

$$\zeta_{\max} = (2g')^{-1}(c_c - q_{\max})^2, \tag{24}$$

where $q_{\max}$ is the maximum value of the drift augmented by the long wave, c_c is the short-wave phase speed at the long-wave crest, and g' is the effective value of gravity for the short waves, $g' = g - a$, where a is the orbital acceleration in the long wave (Longuet-Higgins 1987). Equation (24) means that the short waves will break to give off their energy completely when the fluid particles at the long-wave crest are moving forward with a drift speed greater than the short-wave phase speed.

When the variations in wind stress are neglected and the motion is steady in a frame of reference moving with the long-wave phase speed, the surface drift augmented by long waves, in the first-order approximation of long-wave slope, is (Phillips and Banner 1974)

$$q = (C - u_0 \cos\theta) - [(C - u_0 \cos\theta)^2 - q_0(2C - q_0)]^{1/2}, \tag{25}$$

where u_0 is the amplitude of long-wave orbital velocity component in the alongwind direction, θ is the phase angle of long wave (which equals to zero at crest), C is the long-wave phase speed in the alongwind direction, and q_0 is the surface drift at the point of long-wave profile where the surface displacement $\zeta = 0$.

In the first-order approximation of long-wave slope, the short gravity wave phase speed at the long-wave crest is given (Phillips and Banner 1974) as

$$c_c = c_0(1 - \beta_s), \tag{26}$$

where c_0 is the short-wave phase speed at the point of the long-wave profile where the surface displacement $\zeta = 0$, β_s is the long-wave slope (actually, the amplitude of long-wave slope), $\beta_s = u_0/C$.

The kinematic breaking criterion for short waves at the long-wave crest, expressed by an inequality, is

$$q_{\max} > c_c. \tag{27}$$

From (25) and a few binding relations among the long-wave phase speed, the long-wave orbital velocity, and the surface drift, we found that the maximum value of the surface drift is approximately proportional to the

amplitude of the long-wave orbital velocity (see appendix A). It is expressed as

$$q_{\max} \approx a u_0, \tag{28}$$

where the proportional coefficient a is on the order about 0.15 in the open ocean. The value of a in the wind–wave tunnel is much larger than 0.15.

Relation (26) is derived based on an assumption of conservation of the angular frequency of short waves. This assumption may not be used for the gravity–capillary waves with small phase speeds, especially when the amplitude of the long-wave orbital velocity is great, because there is no real solution (Shyu and Phillips 1990). In the first-order approximation, $g' = g(1 - \beta_s \cos\theta)$, where β_s is the long-wave slope. Influenced by the variation of g', the short-wave phase speed at the crest is

$$c_c = \left[\frac{g'}{k} + \frac{\tau k}{\rho}\right]^{1/2} = \left[\left(\frac{g}{k} + \frac{\tau k}{\rho}\right) - \frac{\beta_s g}{k}\right]^{1/2}$$
$$\approx c - \frac{\beta_s c}{2}\frac{g/k}{g/k + \tau k/\rho} = c - \frac{u_0 c}{2C}\frac{g/k}{g/k + \tau k/\rho}. \tag{29}$$

Substituting (28) and (29) into (27), an equivalent criterion is derived as

$$u_0 > \frac{c}{a\left(1 + \dfrac{c}{2aC}\dfrac{g/k}{g/k + \tau k/\rho}\right)}$$

or

$$u_0 > \frac{c}{a}\left(1 - \frac{c}{2aC}\frac{g/k}{g/k + \tau k/\rho}\right) \approx \frac{c}{a}. \tag{30}$$

For moderate and strong winds in the open ocean, C/c is generally over 50. The second term within brackets in (30) is small and can be neglected. Therefore, the equivalent criterion is expressed, in a roughly approximation, as

$$u_0 > \frac{c}{a}, \tag{31}$$

where a is a parameter related to fetch. It means that if the amplitude of long-wave orbital velocity is over $1/a$ times the short-wave phase speed, the surface drift at the crest, augmented by long waves, will have a speed greater than the short-wave phase velocity, and the short waves will be wiped out by the drift. Because the surface drift partially advects the short waves (Smith 1986), the percentage of the drift that does not take part in the advection should be added in the left side in (31). In a rough approximation, this percentage is assumed to be a constant for short waves near $c_{\min}$, which is about 3.616 rad cm^{-1}. In other words, we may overestimate the suppression by the surface drift for shorter capillary waves under this assumption. Considering the advection, the equivalent criterion should be

$$b u_0 > \frac{c}{a},$$

or

$$u_0 > \alpha_0 c, \tag{32}$$

where $\alpha_0 = 1/ab$ and b is the percentage of the drift that does not take part in the advection.

Supposing an angle ϕ between the short waves and the mean wind direction, a cosine function should be added into (32) such that

$$u_0 \cos\phi > \alpha_0 c. \tag{33}$$

In order to apply the criterion to calculate the influence on the wind-induced wave growth rate from the wave–drift interactions, we must know the probability distribution of the amplitude of long-wave orbital velocities.

With the assumptions that the long-wave orbital velocity component in the alongwind direction is Gaussian and that the corresponding energy spectrum is narrow, the probability density of its distribution can be described (see appendix B) by

$$f(\eta) = \eta \exp\left(-\frac{\eta^2}{2}\right), \tag{34}$$

with

$$\eta = \frac{u_0}{\mu_0^{1/2}},$$

where μ_0 is the zeroth moment of the spectrum of long-wave orbital velocity component in the alongwind direction. An equivalent expression of the criterion (33) is

$$\eta > \frac{\alpha_0 c}{\cos\phi \mu_0^{1/2}}. \tag{35}$$

The probability of short-wave breaking due to the surface drift is

$$P\left(\eta > \frac{\alpha_0 c}{\cos\phi \mu_0^{1/2}}\right) = \int_{\alpha_0 c/(\cos\phi\sqrt{\mu_0})}^{\infty} \eta \exp\left(-\frac{\eta^2}{2}\right) d\eta$$
$$= \exp\left(\frac{-\alpha_0^2 c^2}{2\cos^2\phi\mu_0}\right). \tag{36}$$

The zeroth moment in the alongwind direction is given by (B6) in appendix B as

$$\mu_0 = \int_0^{\infty}\int_{-\pi/2}^{\pi/2} \Phi(\omega, \theta)\cos^2\theta d\theta d\omega \propto m_0, \tag{37}$$

where $\Phi(\omega, \theta)$ is the directional spectrum of long-wave orbital velocity, θ is the angle between the mean wind direction and the long-wave orbital velocity, and m_0 is

the zeroth moment of the nondirectional frequency spectrum of long-wave orbital velocity.

The zeroth moment m_0 is given by (B9) and (B12) in appendix B as

$$m_0 \propto \begin{cases} U^2 & \text{for open ocean,} \\ (u_* - 5 \text{ cm s}^{-1})^2 & \text{for wind–wave tunnel,} \end{cases} \tag{38}$$

where U is the wind speed at a height 10 m or 19.5 m over the ocean surface, u_* is the wind friction velocity, and 5 cm s^{-1} is the threshold friction velocity.

The dissipation due to the wave–drift interactions can be expressed as

$$D = bS_w P\left(\eta > \frac{\alpha_0 c}{\cos\phi \mu_0^{1/2}}\right) = bS_w \exp\left(\frac{-\alpha_0^2 c^2}{2\cos^2\phi\mu_0}\right), \tag{39}$$

where S_w represents the wind input, b represents the absence rate of short waves when the short-wave breaking takes place. The absence rate b refers to a position where the short-wave breaking takes place. For the windward side of long background waves, b is equal to 1. For the leeward side or both sides, b can be assumed to be a function of the probability of short-wave breaking such that

$$b = \left[P\left(\eta > \frac{\alpha_0 c}{\cos\phi\mu_0^{1/2}}\right)\right]^x. \tag{40}$$

Substituting (37) and (40) into (39), we obtain

$$D = S_w \exp(-c^2/\alpha_1 \cos^2\phi\, m_0), \tag{41}$$

where the value of constant α_1 is different when the windward side, the leeward side, or both sides are considered.

In the presence of very strong winds, the serious breaking of short waves can cause turbulence. The turbulence from the breaker destroys all of the short waves in both the alongwind and the crosswind directions. Considering both directions, the dissipation due to the wave–drift interactions should be

$$D = S_w \exp\left(\frac{-c^2}{(\alpha_1 \cos^2\phi + \alpha_2 \sin^2\phi) m_0}\right), \tag{42}$$

where the constants α_1 and α_2 can be determined by measurements. Generally, α_2 is much less than α_1.

4. Spectrum of the gravity–capillary waves

a. Balance of energy

The action spectrum $N(\mathbf{k})$, is defined as

$$N(\mathbf{k}) = c\Phi(\mathbf{k}) = \frac{g_*}{\omega}\Phi(\mathbf{k}) = \frac{g_*}{\omega} k^{-4} B(\mathbf{k}), \tag{43}$$

where $g_* = g + (\tau/\rho)k^2$, g is the gravitational acceleration, τ is the water surface tension, ρ is the water density, k is the wavenumber, c is the intrinsic phase speed of the gravity–capillary waves, $\Phi(\mathbf{k})$ is the wavenumber spectrum, and $B(\mathbf{k})$ is the degree of saturation expressed in terms of a dimensionless function. This equation is from Plant [1986, see his Eq. (1)]. The action is defined as the energy over the frequency. The calculations of the energy for the gravity waves and for the capillary waves have been given by Phillips [1977, see his Eqs. (3.2.7) and (3.2.8)].

Following energy paths, the balance of action spectrum for a state of statistical equilibrium can be represented as

$$\frac{dN}{dt} = -\nabla\cdot\mathbf{T}(\mathbf{k}) + S_w - D = 0. \tag{44}$$

The action spectrum will be determined by the rate of wind input S_w, the spectral flux divergence $\nabla\cdot\mathbf{T}(\mathbf{k})$, and the dissipation D.

b. Three physical processes

The rate of wind input can be determined by

$$S_w = \beta N(\mathbf{k}), \tag{45}$$

where β is the wind-induced wave growth rate. Considering molecular viscosity and eddy viscosity, the wind-induced wave growth rate normalized by angular frequency can be expressed by

$$\frac{\beta}{\omega} = 0.04x^2 \exp\left(\frac{-4\nu_e k^2}{\omega/0.04x^2/\gamma}\right), \tag{46}$$

with

$$x = (u_* - \delta)/c,$$

which is obtained from Eq. (17). Substituting (43) and (46) into (45), we obtain

$$S_w = 0.04 g_* k^{-4} x^2 D_w(\phi) B(\mathbf{k}) \times \exp(-4\nu_e k^2/\omega/0.04x^2/\gamma), \tag{47}$$

where the directional spreading function $D_w(\phi)$ of wind is added.

The spectral redistribution of wave action in the range of gravity waves has been investigated by Hasselmann (1962; 1963a,b) as a "collision integral" over sets of four resonantly interacting gravity waves. This integral is cubic rather than quadratic in wave action $N(\mathbf{k})$, because resonant gravity wave interactions involve sets of four components, rather than three. The result of the integral is given by Kitaigorodskii (1983):

$$\nabla\cdot\mathbf{T}(\mathbf{k}) \propto g^{-1/2} k^{19/2} N^3(\mathbf{k}). \tag{48}$$

This is also expressed by using dimensionless function $B(\mathbf{k})$ (Phillips 1985):

$$\nabla \cdot \mathbf{T}(\mathbf{k}) \propto gk^{-4}B^3(\mathbf{k}). \quad (49)$$

Among very short gravity–capillary waves, for which gravity and surface tension are both important, $\omega = (gk + \tau k^3)^{1/2}$, it is found that the resonance of three components is more significant than that of four components. The details involved have been studied by McGoldrick (1965). Based on analogy, the collision integral over sets of three resonantly interacting gravity–capillary waves is quadratic in action $N(\mathbf{k})$. The spectral flux divergence has dimensional factor $g_* k^{-4}$ and it is expected to be expressed as

$$\nabla \cdot \mathbf{T}(\mathbf{k}) \propto g_* k^{-4} B^2(\mathbf{k}). \quad (50)$$

The dissipation due to the wave–drift interaction is

$$D = S_w \exp[-c^2/(\alpha_1 \cos^2\phi + \alpha_2 \sin^2\phi)m_0], \quad (51)$$

which is from (42).

c. *Spectrum of gravity–capillary waves*

Substituting (47), (50), and (51) into (44), the spectrum of the gravity–capillary waves can be obtained immediately as

$$\Phi(k, \phi) = k^{-4}B(k, \phi) = mk^{-4}x^2 D_w(\phi) \times \exp(-4\nu_e k^2/\omega/0.04x^2/\gamma) \times \{1 - \exp[-c^2/(\alpha_1 \cos^2\phi + \alpha_2 \sin^2\phi)m_0]\} \quad (52)$$

with

$$x = (u_* - \delta)/c,$$

where m is a constant, $D_w(\phi)$ is the directional spreading function of the wind, and x^2 is the wind input combined with dissipation due to the molecular viscosity. Here

$$\exp\left[-\frac{4\nu_e k^2/\omega}{0.04x^2/\gamma}\right]$$

refers to dissipation due to the eddy viscosity, which is significant only for the capillary waves with wavenumbers more than k_m ($k_m = (\rho g/\tau)^{1/2} \approx 361.6$ rad m^{-1}),

$$1 - \exp\left(-\frac{c^2}{(\alpha_1 \cos^2\phi + \alpha_2 \sin^2\phi)m_0}\right)$$

is the factor referring to small wave breaking due to the wave–drift interactions, ν_e is the kinematic eddy-viscosity coefficient of water, and m_0 is the zeroth moment of nondirectional frequency spectrum of long-wave orbital velocity, which is given by (38).

The spectrum of the gravity–capillary waves in the alongwind direction is

$$\Phi(k, 0) = k^{-4}B(k, 0) = mk^{-4}x^2 \exp(-4\nu_e k^2/\omega/0.04x^2/\gamma) \times [1 - \exp(-c^2/\alpha_1 m_0)], \quad (53)$$

with

$$x = (u_* - \delta)/c.$$

The directional spreading function of the gravity–capillary waves is

$$D(\phi) = D_w(\phi) \times \frac{1 - \exp\left[-\dfrac{c^2}{(\alpha_1 \cos^2\phi + \alpha_2 \sin^2\phi)m_0}\right]}{1 - \exp\left(-\dfrac{c^2}{\alpha_1 m_0}\right)}. \quad (54)$$

It means that both the wind direction distribution and the wave–drift interaction determine the directional behavior of the gravity–capillary waves. Equation (54) indicates that $D(\phi)$ will be wider when m_0/c^2 becomes larger.

The threshold friction velocity δ is empirically determined to be about 5 cm s^{-1}, which corresponds a value of about 1.3 m s^{-1} for wind at 10 m over the water surface. The physical reason for this selection will be discussed in section 4e. For fully developed waves, the value of γ is different from that in the initial stage, such as presented in Eq. (17); γ is related to the variance of the local wind friction velocity. The variance of the local wind friction velocity in the fully developed stage is different from that in the initial stage.

The degree of saturation $B(k, \phi)$ as used in (52) is approximately equal to "curvature spectrum." Hence the term "saturation spectrum" [$B(k, \phi)$] can be replaced by "curvature spectrum," as suggested by Apel (1994).

d. *Comparison with laboratory measurements*

For a narrow wind–wave tunnel, the zeroth moment m_0 of the nondirectional frequency spectrum of long-wave orbital velocity is proportional to the wind stress input. Substituting the second expression in (38) into (53) and (54), the spectrum of the gravity–capillary waves in the alongwind direction can be expressed as

$$\Phi(k, 0) = k^{-4}B(k, 0) = mk^{-4}x^2 \exp(-4\nu_e k^2/\omega/0.04x^2/\gamma) \times [1 - \exp(-1/\alpha_1 x^2)], \quad (55)$$

with

$$x = (u_* - \delta)/c,$$

and the directional spreading function of the gravity–capillary waves can be expressed as

$$D(\phi) = D_w(\phi) \times \frac{1 - \exp\left[-\dfrac{1}{(\alpha_1 \cos^2\phi + \alpha_2 \sin^2\phi)x^2}\right]}{1 - \exp\left(-\dfrac{1}{\alpha_1 x^2}\right)}. \quad (56)$$

In order to fit the measurements by Jähne and Riemer (1990), some parameters are given as follows:

(i) The proportional coefficient of the spectrum of the gravity–capillary waves

$$m = \frac{1}{320}.$$

(ii) The eddy viscosity coefficient together with the dimensionless coefficient γ

$$\gamma\nu_e = 3.6 \times 10^{-6}\omega^{1.5}\left(\frac{u_* - \delta}{c}\right)^{2.5}.$$

(iii) The threshold wind friction velocity

$$\delta = 5 \text{ cm s}^{-1}.$$

(iv) The parameters related to fetch

$$\alpha_1 = 0.225, \quad \alpha_2 = 0.025.$$

(v) The directional spreading function of the wind

$$D_w = \exp(-1.05|\phi|), \quad \text{for} \quad -\pi \leq \phi \leq \pi.$$

Comparison of the degree of saturation given by (55) with the measurements of Jähne and Riemer (1990) is shown in Fig. 3 over a wide wavenumber range for short waves. Figure 3 shows that the eddy-viscous dissipation plays the main role in the cutoff range over $k = 1000$ rad m^{-1} and at higher wind friction velocities. In other words, the dynamical reason for the spectral cutoff of the ripples is due to the eddy viscosity. The maximum degree of saturation given by (55) is present near the wavenumber k_m ($k_m = (\rho g/\tau)^{1/2}) \approx 361.6$ rad m^{-1}). The wind stress input causes a peak at k_m in the spectral curves. The factor within brackets in (55) suppresses the peaks in the spectral curves at higher wind speeds. For shorter fetch, the background waves and the drifts are not so strong, and the peaks in the spectral curves will then be obvious.

For convenience of comparison with measurements, Eq. (55) can be changed from its original form into the following form:

$$B(k, 0)\exp(4\nu_e k^2/\omega/0.04x^2/\gamma) = mx^2[1 - \exp(-1/\alpha_1 x^2)]. \quad (57)$$

It means that the right side of (57) represents the degree of saturation without eddy-viscous dissipation. The factor of eddy-viscous dissipation was moved into the left side of the above equation. Figure 4 gives a comparison of Eq. (57) with the measurements of Jähne and Riemer (1990) over the wavenumber range from 141.4 rad m^{-1} to 600 rad m^{-1}. Figure 5 gives a comparison of Eq. (57) with measurements over a wavenumber range from 40 rad m^{-1} to 1414 rad m^{-1}. At lower winds, the degree of saturation is very well described

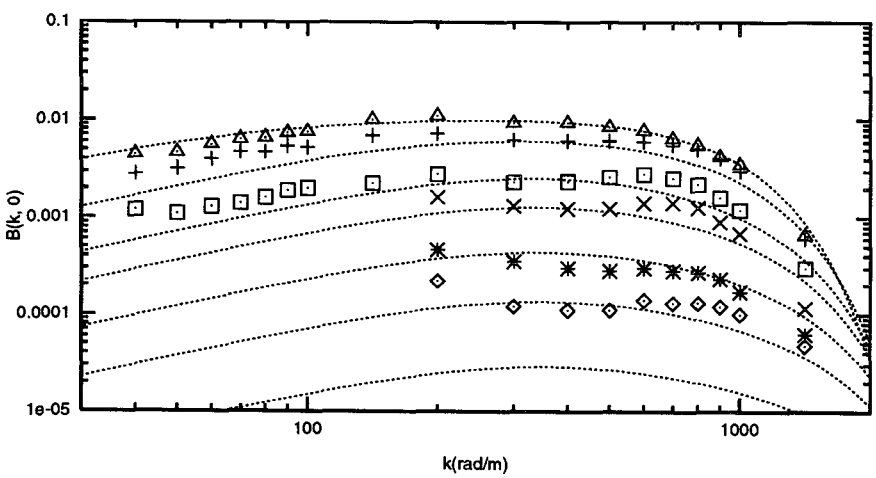

FIG. 3. The degree of saturation versus the wavenumber—a comparison of the spectrum of the gravity–capillary waves in alongwind direction (0 ± 5°) given by Eq. (55) with the measurements by Jähne and Riemer (1990). The dashed lines from upper to lower, corresponding to the friction velocities 0.722, 0.424, 0.269, 0.205, 0.140, 0.100, and 0.073 m s^{-1}, respectively, are given by Eq. (55). The others are from the measurements for the same velocities. The triangles correspond to 0.722 m s^{-1}, the plus signs 0.424 m s^{-1}, the squares 0.269 m s^{-1}, the crosses 0.205 m s^{-1}, the asterisks 0.140 m s^{-1}, and the diamonds 0.100 m s^{-1}. The measurements at 0.073 m s^{-1} and near the spectral peaks are not presented.

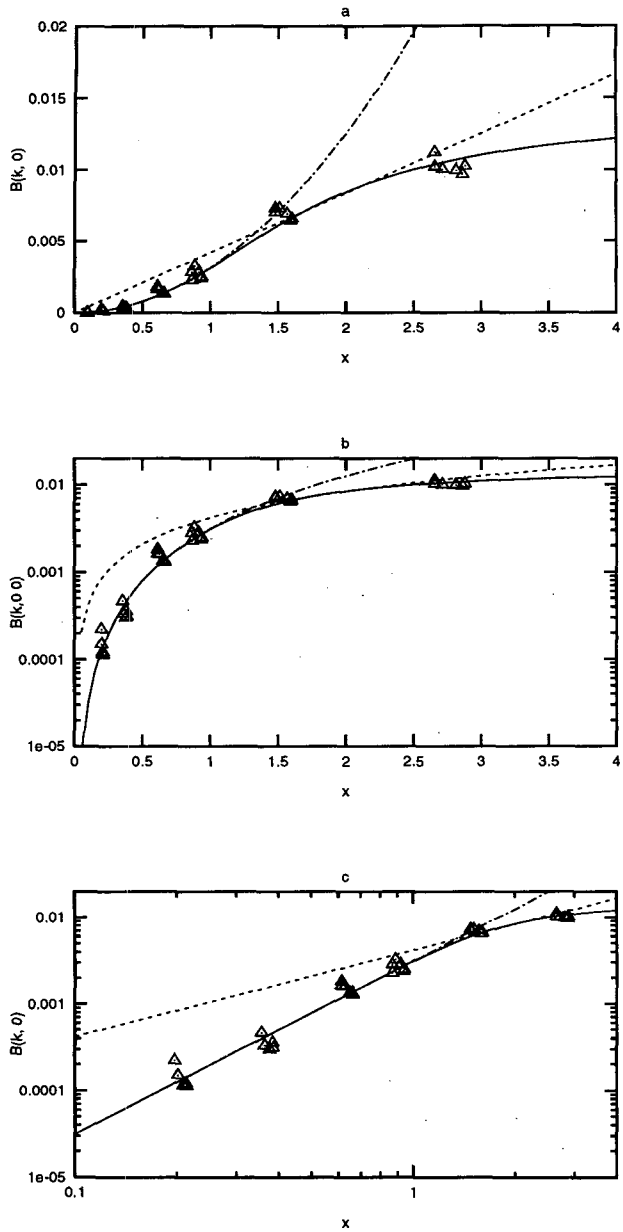

FIG. 4. The degree of saturation vs $(u_* - \delta)/c$—a comparison of the spectrum of the gravity–capillary waves in alongwind direction ($0 \pm 5°$) by Eq. (57) with the measurements by Jähne and Riemer (1990). The degree of saturation without eddy-viscous dissipation, represented by solid lines, is calculated from the right side of Eq. (57). The degree of saturation with only molecular-viscous dissipation, represented by dashed–dot lines, is calculated from mx^2. The degree of saturation with a linear relation to the wind friction velocity, represented by dashed lines, is calculated from $m'x$, where $m' = 1/120$ and $x = (u_* - \delta)/c$. The triangles represent the measurements in a wavenumber range from 141.4 rad m^{-1} to 600 rad m^{-1}. To compare with the degree of saturation calculated from the right side of Eq. (57), the data, measured by Jähne and Rimer (1990), were added eddy-viscous losses by using the left side of Eq. (57). The three different coordinate scales are given: (a) natural coordinates, (b) logarithmic y versus natural x coordinate, (c) double logarithmic coordinates.

by $x^2 = [(u_* - \delta)/c]^2$. At higher winds, the modulation from wave–drift interactions suppresses the energy of the short waves and plays a significant role.

Figure 6 gives a comparison of the directional spreading function (56) with the measurements of Jähne and Riemer (1990) at $\phi = 60 \pm 5°$ and $90 \pm 5°$, respectively, at higher winds. The modulation from wave–drift interaction widens the distribution of the gravity–capillary waves. This comparison is only a reference, because the information on the directional distribution of wind input is not available.

For the open ocean, the zeroth moment m_0 of the nondirectional frequency spectrum of long-wave orbital velocity is proportional to the square of wind speed at a height over the ocean surface. Further, the wind speed is proportional to the phase speed of dominant long waves at spectral peak. Substituting the first expression in (38) and (A1) into (54), we have

$$D(\phi) = D_w(\phi) \frac{1 - \exp\left[-\dfrac{(c/C)^2}{\alpha_1 \cos^2\phi + \alpha_2 \sin^2\phi}\right]}{1 - \exp\left[-\dfrac{(c/C)^2}{\alpha_1}\right]}, \tag{58}$$

where C/c is the ratio of the phase speed of dominant long waves to that of short waves. For short gravity waves, $(C/c)^2 \approx k/k_p$, where k is the wavenumber of short gravity waves, and k_p is the wavenumber of long waves at spectral peak. Donelan et al. (1985) and Banner (1991) found that the ratio k/k_p controls the rate of spreading of short gravity waves as a function of the distance from the spectral peak. Equation (58) gives a possible physical explanation to the directional behavior of short gravity waves.

e. *Threshold friction velocity*

In section 4d, the threshold friction velocity δ for fully developed waves is empirically determined to

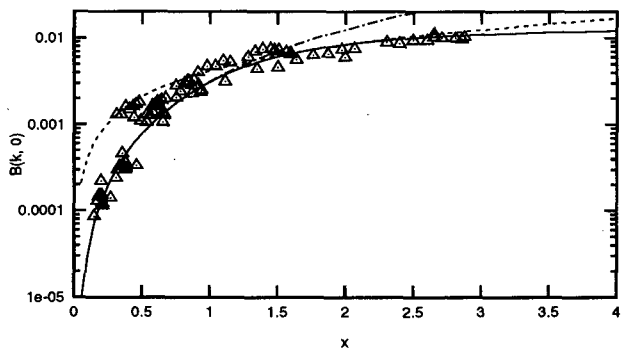

FIG. 5. The same as in Fig. 4b except for the wavenumber range of the measurements. The data are the same as in Fig. 3; the wavenumber range is from 40 rad m^{-1} to 1414 rad m^{-1}.

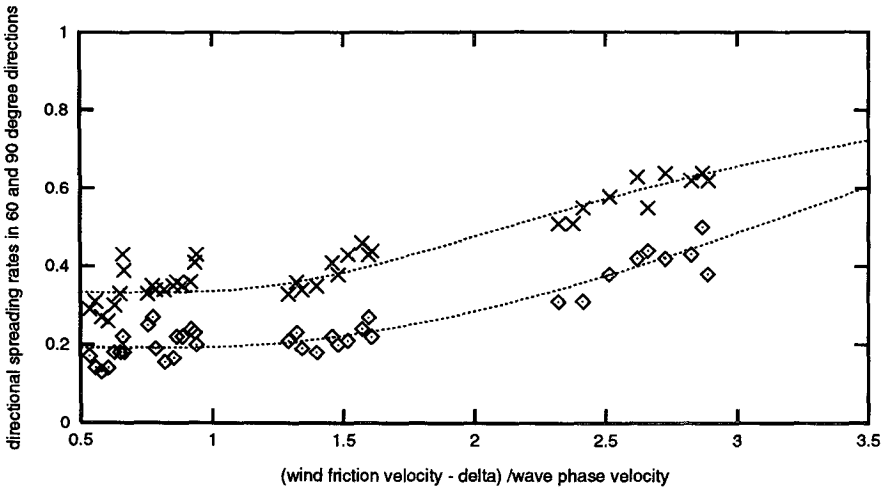

FIG. 6. The directional spreading function averaged in 60 ± 5° and 90 ± 5° vs $(u_* - \delta)/c$—a comparison with the measurements. The upper and lower lines, inferred from (56), represent the directional spreading rates averaged in 60 ± 5° and 90 ± 5°, respectively. The crosses and rhombuses represent the measurements by Jähne and Riemer (1990).

be about 5 cm s^{-1}. It is different from the empirical relation of threshold friction velocity in the initial stage, which is given in (17). In the initial stage, wind stress fluctuation is generated only by the atmosphere. In the fully developed stage, other sources of energy input are added and the wind stress fluctuation is generated by both the atmospheric turbulence and the background waves in the water. A few possible sources of energy input for capillary waves are found to be complementary. Capillary wave generation at the steep wave crest in the absence of wind has been demonstrated in an experiment of Cox (1958). The generation of capillary waves is due to the high curvature at the crest of underlying gravity waves and the action of "radiation stress" (Longuet-Higgins 1963). This mechanism suggests that the capillary waves extract energy from the primary waves with wavelengths 5–30 cm. Second, some capillary waves may be maintained by the second-order wave–wave interactions giving an energy flux from spectral components more adequately supplied with energy from the wind (Phillips 1977). The feature of the bimodal angular dispersion at lower winds, observed by Jähne and Riemer (1990), supports this mechanism. Finally, we suggest that the additional wind Reynolds stress fluctuations, which are generated by the background waves and related to the time and space scales of doing work, are a possible reason. It is estimated that the required scales averaged in time and space are different for different capillary waves with different wavelengths. The Reynolds stress fluctuations generated by water waves will be stronger, if the required averaged scales are smaller.

The threshold friction velocity δ is determined by a balance between the wind input and the molecular-viscous dissipation. The wind input is related to the wind Reynolds stress fluctuations. The wind Reynolds stress fluctuations are generated by atmospheric turbulence and dominant water waves. The scale of the dominant water waves is smaller than that of the atmospheric turbulence. It is estimated that the wind Reynolds stress fluctuations generated by dominant water waves are different for capillary waves with different wavelengths. The reason is that the scale of the dominant water waves is not too large compared with the scale required to complete doing works for capillary waves. In the initial stage, the dominant water waves are not formed. Therefore, the wind stress fluctuations and wind input in the initial stage and in the fully developed stage are different from each other. This difference causes different threshold friction velocities for different stages.

5. Comparison with field measurements

a. Spectrum of the gravity–capillary waves in the open ocean

For the open ocean, the zeroth moment m_0 of the nondirectional frequency spectrum of long-wave orbital velocity is proportional to the square of wind speed at 10 m over the ocean surface. Substituting the first expression in (38) into (53) and (54), the spectrum of the gravity–capillary waves can be expressed as

$$\Phi(k,\phi) = mk^{-4}\left(\frac{u_* - \delta}{c}\right)^2\left[1 - \exp\left(\frac{-c^2}{\alpha_1 U_{10}^2}\right)\right]D(\phi), \quad (59)$$

with the directional spreading function of the gravity–capillary waves given by

$$D(\phi) = \frac{1 - \exp\left[-\dfrac{c^2}{(\alpha_1 \cos^2\phi + \alpha_2 \sin^2\phi)U_{10}^2}\right]}{1 - \exp\left(-\dfrac{c^2}{\alpha_1 U_{10}^2}\right)} D_w(\phi),$$

and the directional spreading function of the wind stress input as

$$D_w(\phi) = \operatorname{sech}^2(h\phi).$$

This spectrum is suitable for K_u-band and C-band. For K_a-band, eddy-viscous dissipation should be added. In order to fit the field data obtained from K_u-band measurements and C-band empirical models, the parameters are as follows:

(i) The proportional coefficient of the spectrum of the gravity–capillary waves

$$m = \frac{1}{280}.$$

(ii) The threshold wind friction velocity

$$\delta = \begin{cases} 3.0 \text{ cm s}^{-1} & \text{for C-band} \\ 5.0 \text{ cm s}^{-1} & \text{for } K_u\text{-band} \end{cases}$$

(iii) The parameters due to the wave–drift interactions

$$\alpha_2 = 0.00005 \times 1.2^2,$$

$$\alpha_1 = \begin{cases} 0.0003 \times 1.2^2 & \text{for the leeward side of the background waves,} \\ 0.0006 \times 1.2^2 & \text{for the windward side of the background waves} \end{cases}$$

(iv) The parameter in the wind stress directional distribution is

$$h = 1.4.$$

The relationship between u_* and U_{10} is

$$\tau_0 = \rho_a u_*^2 = \rho_a C_d U_{10}^2, \tag{60}$$

where C_d is the neutral-stability drag coefficient, which is used in (59) to obtain the wind friction velocity from the wind speed at 10 m over the ocean surface. The drag coefficient used here is (Pierson et al. 1984)

$$C_d = 10^{-3}(2.717U_{10}^{-1} + 0.142U_{10}^{-1} + 0.0761U_{10}), \tag{61}$$

which is based on the data of Large and Pond (1981), Davidson et al. (1981), and Dittmer (1977).

b. Backscatter theory

A way of comparing our model to field measurements is to examine the agreement or the difference between the radar backscatter cross sections (RBCS) measured in the open ocean and the theoretical radar backscatter values calculated from the backscatter theory and the spectrum of the gravity–capillary waves.

The total energy of radar backscatter by the ocean surface includes two parts: one from Bragg resonance, the other from specular reflection. In the two-scale model, radar backscatter cross sections due to Bragg resonance of the first order (Wright 1968; Valenzuela 1978; Brown 1978; Stewart 1985) for vertical polarization are

$$\sigma_0^i = 16\pi k_R^4 \left| \left(\frac{\alpha \cos\delta}{\alpha_i}\right)^2 g_{vv}^{(1)}(\theta_i) + \left(\frac{\sin\delta}{\alpha_i}\right)^2 g_{hh}^{(1)}(\theta_i) \right|^2 \Phi \times \left[2k_R \sin\theta_i, \phi + \tan^{-1}\left(\frac{\gamma \sin\delta}{\alpha}\right)\right], \tag{62}$$

where k_R is the radar wavenumber and $g_{vv}^{(1)}(\theta)$ and $g_{hh}^{(1)}(\theta)$ are the first-order scattering coefficients for vertical polarization and for horizontal polarization, respectively, given by

$$g_{vv}^{(1)}(\theta_i) = \frac{(\epsilon_r - 1)[\epsilon_r(1 + \sin^2\theta_i) - \sin^2\theta_i]\cos^2\theta_i}{[\epsilon_r \cos\theta_i + (\epsilon_r - \sin^2\theta_i)^{1/2}]^2},$$

$$g_{hh}^{(1)}(\theta_i) = \frac{(\epsilon_r - 1)\cos^2\theta_i}{[\cos\theta_i + (\epsilon_r - \sin^2\theta_i)^{1/2}]^2},$$

where ϵ_r is the complex dielectric constant, which can be calculated from the Debye equation (Stewart 1985; Klein and Swift 1977), θ_i is the local incidence angle, $\Phi[2k_R \sin\theta_i, \phi + \tan^{-1}(\gamma \sin\delta/\alpha)]$ is the two-dimensional (polar coordinate) wavenumber spectrum of the gravity–capillary waves, $2k_R \sin\theta_i$ is the wavenumber of Bragg resonance, ϕ is the azimuth angle between the upwind direction and the projection of radar beam in the ocean surface, and $\tan^{-1}(\gamma \sin\delta/\alpha)$ is the variety of azimuth angle caused by local surface slopes. The relevant four variables are

$$\alpha_i = \sin\theta_i,$$

$$\alpha = \sin(\theta + \psi),$$

$$\gamma = \cos(\theta + \psi),$$

$$\cos\theta_i = \cos(\theta + \psi)\cos\delta,$$

where ψ and δ are the local ocean surface slopes, which can be calculated from

$$\sin\delta = \sin\psi_b \sin\phi,$$

$$\tan\psi = \tan\psi_b \cos\phi, \tag{63}$$

where ψ_b is the mean tilt of leeward side or windward side of the background waves. The value of ψ_b is given by

$$\tan\psi_b = \pm\int_0^{\tan(\pi/6)} xdx \int_{-\infty}^{\infty} f(x, y)dy, \quad (64)$$

where $f(x, y)$ is the joint probability density of the slopes. The sum of RBCS due to Bragg resonance in both sides of the background waves is

$$\sigma_0^B = \frac{1}{2}\sigma_0^{\text{leeward}} + \frac{1}{2}\sigma_0^{\text{windward}}, \quad (65)$$

where 1/2 is the probability of small waves in leeward side or windward side of the background waves. This is a simple two-scale model, which produces a small difference between the values of RBCS from the upwind direction and the downwind direction.

The radar backscatter cross sections (RBCS) due to specular reflection (Barrick 1968; Valenzuela 1978; Apel 1987) are

$$\sigma_0^R = \pi \sec^4\theta f(\zeta_x, \zeta_y)|R(0)|^2, \quad (66)$$

where θ is the incidence angle of the radar beam and $|R(0)|^2$ is the Fresnel reflection coefficient for normal incidence (Stewart 1985; Schanda 1976). In (66), the joint probability density of slopes $f(\zeta_x, \zeta_y)$ is evaluated at the specular points; ζ_x and ζ_y are the slopes of the rough surface in the upwind and the crosswind directions at the specular points. For a wide spectrum, the nonlinear interactions cannot be neglected, and the slopes cannot be described by a Gaussian distribution. Considering nonlinear wave–wave interactions, the joint probability density of slopes is given by Liu (1995, unpublished manuscript)

$$f(x, y) = \frac{n}{2\pi(n-1)\sigma_x\sigma_y}\left[1 + \frac{x^2}{(n-1)\sigma_x^2} + \frac{y^2}{(n-1)\sigma_y^2}\right]^{-n+2/2} + \text{skewness}, \quad (67)$$

where x and y are the values of random variables ζ_x and ζ_y, and n is the parameter related to spectrum width. The value of n is selected as 5 for comparison with *ERS-1* models and 100 ($n = 100$ corresponds a narrow spectrum) for comparison with K_u-band data measured by Jones et al. (1977). Here σ_x and σ_y are given by

$$\sigma_x^2 + \sigma_y^2 = \sigma^2, \qquad \frac{\sigma_x^2}{\sigma_y^2} = 0.9, \quad (68)$$

where σ is the "measured" mean square slope, which is given by Wu (1994),

$$\sigma^2 = (0.90 + 1.20 \ln U_{10}) \times 10^{-2}. \quad (69)$$

A mixed model of the "effective" radar backscatter due to both specular reflection and Bragg resonance is

$$\sigma_0 = \sigma_0^R \times r + \sigma_0^B \times P, \quad (70)$$

where r is the effective reflectivity coefficient based on the calibration requirement (Apel 1994; Wu 1994), and its value is selected as 1.0 for comparison with *ERS-1* C-band empirical models and 0.5 for comparison with K_u-band data measured by Jones et al. (1977) in this study. Here P is the probability in which the radar beam involves Bragg resonance:

$$P = \begin{cases} 1 - \dfrac{f(\sqrt{\zeta_x^2 + \zeta_y^2} = \tan\theta)}{f(\sqrt{\zeta_x^2 + \zeta_y^2} = \tan 15°)} & \text{for} \quad \theta > 15° \\ 0 \quad \text{for} \quad \theta < 15°, \end{cases} \quad (71)$$

where f is the joint probability density of slopes, ζ_x and ζ_y are the slopes in x and y directions, and θ is the incidence angle. Actually, the effect of P in this model can be neglected for $\theta > 20°$. Equation (71) is a simplified expression and it is not very accurate. A more accurate expression will be given by Liu.

c. *Comparison with K_u-band measurements—an examination of the proposed spectrum at strong winds*

It is especially significant to compare the spectrum model with field measurements in strong winds. Previous researchers (Phillips 1988; Plant 1986) have obtained a good agreement between their models and field measurements except in the case of strong winds. The measurements by Jones et al. (1977) were for K_u-band and for conditions differing from weak to very strong winds. These data are used to confirm the proposed spectrum (59) by using RBCS calculated from (65) in Fig. 7a and by using RBCS calculated from (70) in Fig. 7b. To emphasize the contribution from the proposed spectrum, the two-scale model related to Bragg resonance and the skewness of the slope distribution related to specular reflection are not adopted in these figures. A similar comparison with the same data was given by Apel (1994). Generally speaking, his model fits the data successfully; the mean error and the standard deviation are quite small. But there are obvious systematic errors in the case of strong winds. The RBCS calculated from his spectrum are smaller than those from data at $U_{19.5} = 23.6$ m s^{-1}, and larger than those from data at $U_{19.5} = 15.0$ m s^{-1}, or 13.5 m s^{-1}. Figure 7 does not show any evidence of systematic errors, which means that the proposed spectrum is an improvement over previous models in the case of strong winds. This improvement is a result of the dissipation mechanism due to wave–drift interactions.

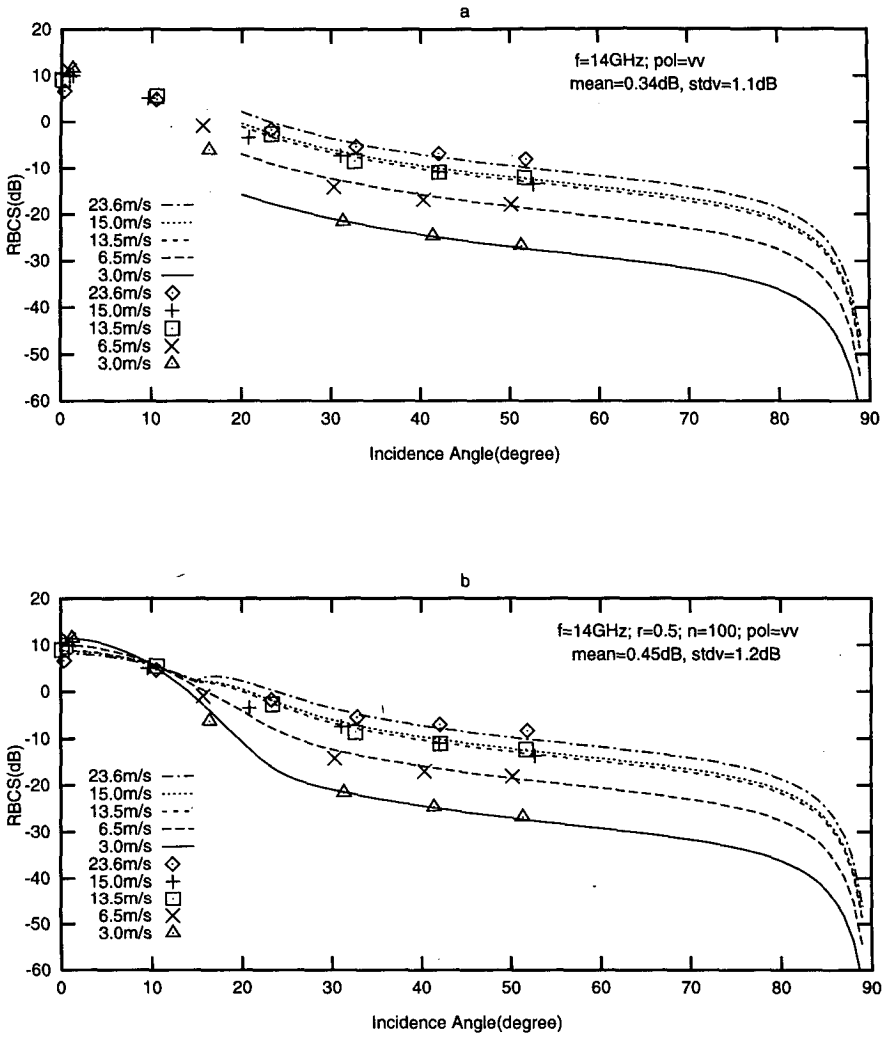

FIG. 7. Calculated and measured radar backscatter cross sections (RBCS) for vertically polarized 14-GHz radar in upwind direction as a function of incidence angle, with wind speed as a parameter. Measurements are from Jones et al. (1977). The lines represent the RBCS calculated from the proposed spectrum and the radar backscatter theory. (a) The RBCS—calculated from Eqs. (62)–(65) and (59), including only the contribution from Bragg resonance. (b) The RBCS—calculated from (70), (66)–(69), (62)–(65), and (59), including the contributions from both Bragg resonance and specular reflection.

Some disagreements from $\theta = 10°$ to $\theta = 25°$ in Fig. 7b are from the selection of probability P in the simple mixed model (70) rather than the proposed spectrum model.

d. *Comparison with C-band empirical models—an examination of the directional spreading function of the proposed spectrum*

The *ERS-1* satellite, launched by the European Space Agency (ESA) on 17 July 1991, has a scatterometer onboard as part of its total sensor package. The scatterometer is an active C-band radar of 5.3 GHz for vertical polarization. The first model of the ocean surface wind recovery algorithm CMOD-1 (Long 1986) for scatterometer data on *ERS-1*, resulting from many aircraft circle-flight campaigns in the North Atlantic, was used in final stages of *ERS-1* design. The second model CMOD-2 (Hoffman 1993), resulting from two datasets (the North Atlantic and the Mediterranean Sea aircraft circle-flight campaigns), was used as prototype for a future space-derived model. Better current models, CMOD-3, CMOD-4, and CMOD-5, etc., based on *ERS-1* data with accuracy about ±0.2 dB, were developed by investigators of ESA, the European Centre for Medium-Range Weather Forecasts (ECMWF), National Aeronautics and Space Administration–Jet Propulsion Laboratory/Oregon State University, and the University of Hamburg (Attema

1992; Hoffman 1993; Anderson et al. 1991; Stoffelen et al. 1992). The model CMOD-3, originating from ECMWF (Stoffelen et al. 1992a,b), has been in use in all stations since 10 July 1992. Six models were evaluated by the National Meteorological Center (NMC), NOAA. Preliminary analysis indicates that the ESA's CMOD-4 operational algorithm (developed at ECMWF) is a leading candidate for implementation at NMC (Woiceshyn et al. 1993).

The CMOD-3 formulas, used in this paper, were from Guignard (1992), the formulas for CMOD-4 were provided by Scott R. Dunbar (1994, personal communication), and those for CMOD-5 were from Quilfen (1993). These models are the result of data from many field measurements, and hence they represent the field measurements.

Figure 8a gives a comparison of the radar backscatter cross sections (RBCS), calculated from Eq. (70), with the data calculated from CMOD-3 in the upwind direction. Figure 8b divides the RBCS into two parts: solid lines representing contributions only from Bragg resonance, dashed lines representing contributions only from specular reflection. Figure 8b shows that Bragg resonance plays a significant role when the incidence angle θ is larger than 35°, and both mechanisms play significant roles when θ is between 18° and 35°. For strong winds, Bragg resonance is more significant for the total range of incidence angles larger than 18°. Figures 9, 10, and 11 give the comparison of RBCS, calculated from the mixed model (70), which includes contribution from the proposed spectrum, with the data from CMOD-3, CMOD-4, and CMOD-5. It is equiv-

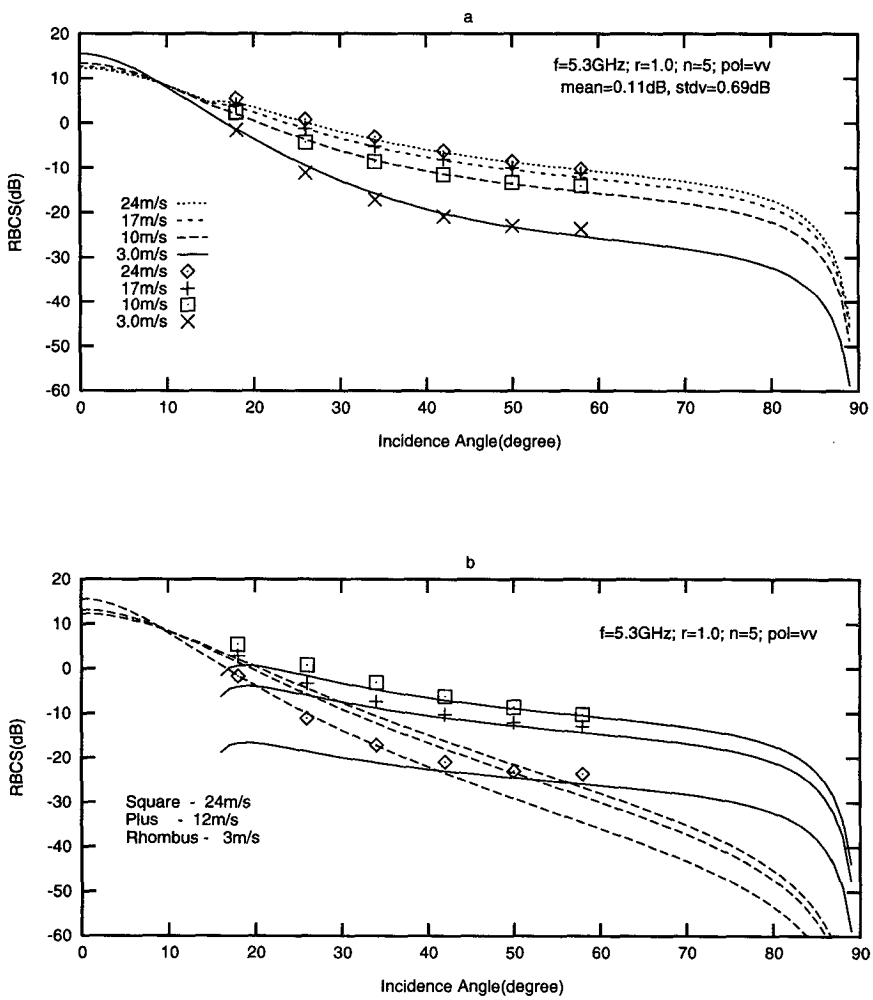

FIG. 8. (a) Calculated and indirectly measured radar backscatter cross sections (RBCS) for vertically polarized 5.3-GHz radar in upwind direction as a function of incidence angle, with wind speed as a parameter. The indirectly measured RBCS, represented by discrete symbols, are from CMOD-3. The RBCS, represented by lines, are calculated from the proposed spectrum and the radar backscatter theory. (b) Similar to (a) except the calculated RBCS are divided into two parts. Solid lines represent the RBCS calculated from Bragg resonance, and dashed lines that from specular reflection.

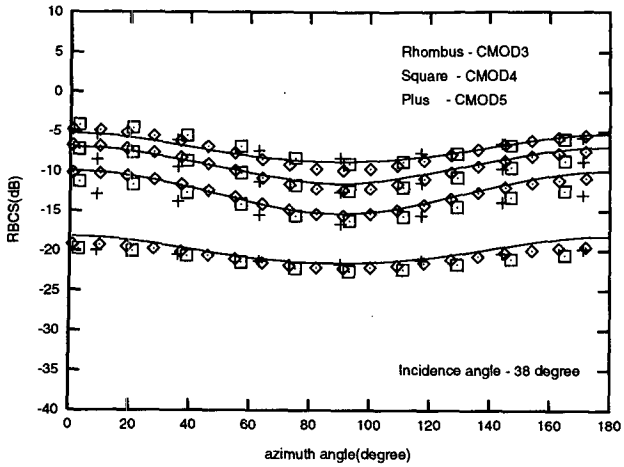

FIG. 9. Calculated and indirectly measured radar backscatter cross sections (RBCS) for vertically polarized 5.3-GHz radar at an incidence angle of 38° as a function of azimuth angle, with wind speed as a parameter. The indirectly measured RBCS are from CMOD-3, CMOD-4, and CMOD-5, and represented by rhombuses, squares, and pluses, respectively. The wind speeds at 10 m over sea surface are 3 m s^{-1}, 10 m s^{-1}, 17 m s^{-1}, and 24 m s^{-1} from lower to upper, respectively. The calculated RBCS, represented by lines, are from the proposed spectrum and the radar backscatter theory.

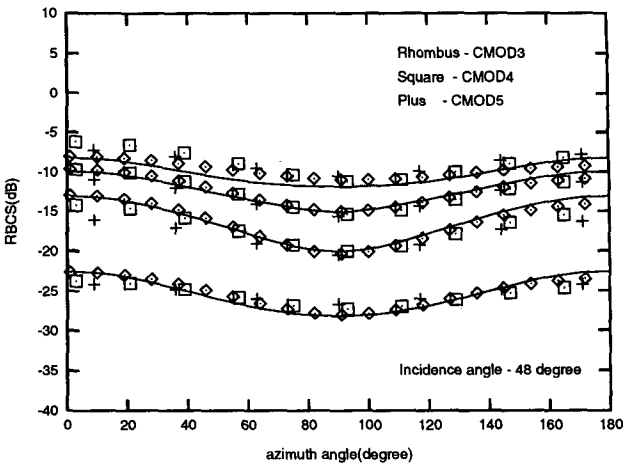

FIG. 10. Similar to Fig. 9 except at an incidence angle of 48°.

alent to compare the proposed spectrum with the field measurements indirectly. To emphasize the contribution from the proposed spectrum, the influence from background waves in the two-scale model related to Bragg resonance and the skewness of the slope distribution related to specular reflection were not shown in these figures. So, the differences between the calculated RBCS at upwind and downwind directions are not shown in these figures.

These figures show good agreements between the proposed spectrum and the field measurements. In comparison with *ERS-1* scatterometer models, the directional spreading function in the proposed spectrum (59) is found to be in agreement with the field measurements indirectly. The directional spreading function is a sum of the directional distribution from the original wind stress input and the modification from wave–drift interactions. Eddy-viscous dissipation is effective only in the range of very high frequencies. This is expected to be confirmed by a comparison with the field measurements in K_a-band at high wind speeds.

The comparisons not only confirm the directional spreading function of the proposed spectrum, but also connect the empirical models with related physical processes. By using Monte Carlo simulations, Liu and Pierson (1994) confirmed that rather small errors in the shape of the wind recovery algorithm curves for C-band backscatter can result in unacceptable systematic errors in both wind speed and direction. Also, raw data from field measurements show radar backscatter to be variable under the same conditions of wind speed and direction. These problems require that we focus our attention on the physical nature of the backscatter. Study of the proposed spectrum model is the first step in this research.

6. Conclusions

Based on the balance of the five physical processes—the wind input, the spectral flux divergence, the dissipation due to molecular viscosity, the dissipation due to eddy viscosity, and the modulation due to wave–drift interaction, a form of the directional spectrum of the gravity–capillary waves is suggested. Following the related theories and the comparisons with measurements, our conclusions are the following:

1) Each physical process plays a special role in setting the wind-induced wave growth rate and the shape of the gravity–capillary wave spectrum. In the suggested spectrum, the wind input with a selected value

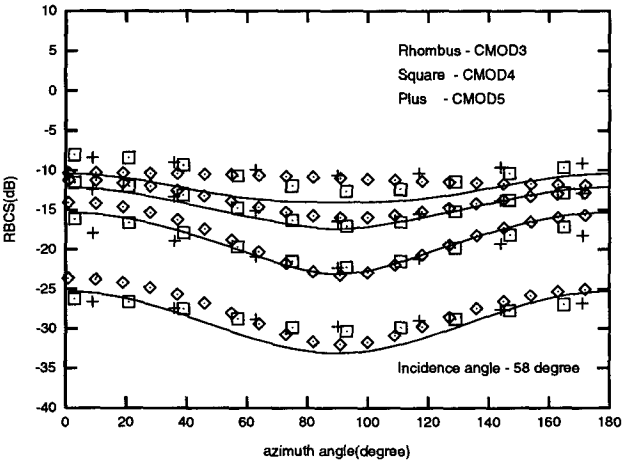

FIG. 11. Similar to Fig. 9 except at an incidence angle of 58°.

of the threshold wind friction velocity controls the energy level in the range of middle and low wind speeds. Both the quadratic relation of wind input and the threshold wind friction velocity controls the slope of the curve of the spectrum versus the wind input. The eddy-viscous dissipation makes the spectrum fit the measurements very well in the range of both higher wind speeds and higher wavenumbers, especially in the "cutoff" range of the spectrum. The modulation from the surface drift has the effect of suppressing the spectrum at higher wind speeds and yields a good agreement with the measurements of both the spectral energy and the directional spreading rate.

2) The physical process involved in the modulation from surface drift has been investigated by Phillips and Banner (1974). Their kinematic breaking criterion is applied in our study of the short-wave dissipation in a very rough approximation and a very simple form. The surface drift augmented by long waves is empirically found to be proportional to the long-wave orbital velocity. So the comparison between the short-wave phase speed and the drift in the criterion can be replaced by the comparison between the short-wave phase speed and the long-wave orbital velocity in an equivalent criterion. The amplitude of long-wave orbital velocity obeys Rayleigh distribution approximately. The probability of short-wave breaking at the crest of long waves has been derived from the equivalent criterion and the distribution of the amplitude of long-wave orbital velocity. The short-wave dissipation is a product of the wind input, the probability of short-wave breaking and the absence rate, which refers to a position of short-wave breaking. The absence rate is assumed to be a function of the probability of short-wave breaking at the crest. Finally, the short-wave dissipation in the alongwind direction is derived as

$$D = S_w \exp(-c^2/\alpha_1 m_0),$$

where m_0 is the zeroth moment of nondirectional frequency spectrum of long-wave orbital velocity, α_1 is a constant, c is the short-wave phase speed, and S_w is the wind input. Further study indicated that the zeroth moment can be estimated by the wind speed in the open ocean or the wind friction stress in the wind wave tunnel.

3) The threshold friction velocity δ is empirically determined to be about 5 cm s^{-1}, which corresponds to a value of about 1.3 m s^{-1} for the wind at 10 m over the water surface in a fully developed stage. In the initial stage, a relation on the threshold friction velocity is obtained from a balance between the molecular-viscous dissipation and the wind input, with consideration of the wind Reynolds stress fluctuation generated by atmospheric turbulence. Physically, the threshold friction velocity δ is determined by a balance between the wind input and the molecular-viscous dissipation. The wind input is related to the wind Reynolds stress fluctuations. The wind Reynolds stress fluctuations are generated by both the atmospheric turbulence and the dominant water waves. The scale of the dominant water waves is smaller than that of the atmospheric turbulence. In the initial stage, the dominant water waves are not formed. Therefore, the wind stress fluctuations and wind input in the initial stage and in the fully developed stage are different from each other. This difference causes different threshold friction velocities for different stages.

4) An equation of the wind-induced wave growth rate is obtained by considering the wind stress fluctuation and the three dissipation processes due to the molecular viscosity, the eddy viscosity, and the wave–drift interaction. Two alternate equations are suggested to simplify the original one.

Acknowledgments. We are very grateful to Professor Willard J. Pierson Jr. and Professor Owen M. Phillips for their helpful advice. We thank Mr. Louis Keiner, Dr. Mohanachandran G. Menon, Mr. Henry Konstanty, and Dr. Richard Field for their assistance in the modification of the manuscript. This work was partially supported by the National Science Foundation under Contract OCE-9453499.

APPENDIX A

The Relationship between the Surface Drift and the Long-Wave Orbital Velocity

At first, we give a few binding relations among the long-wave phase speed, the long-wave orbital velocity, and the surface drift.

From the Neumann spectrum (Neumann 1953), the P–M spectrum (Pierson and Moscowitz 1964), and the spectrum given by Donelan et al. (1985), the dominant long-wave phase speed is found to be proportional to the wind speed at a given height. For example, the P–M spectrum gives

$$C = \frac{U_{19.5}}{0.877}, \tag{A1}$$

where C is the phase speed of dominant long waves at spectral peak and $U_{19.5}$ is the wind speed at 19.5 m over the ocean.

The magnitude of the surface drift is on the order $^3/_{100}$ or $^4/_{100}$ of the mean wind speed as usually measured at a height of 10 m (Banner and Phillips 1974). Because there is only a small difference between U_{10} and $U_{19.5}$, an approximate relation can be given as

$$q_0 = \left(\frac{3.5}{100}\right) U_{19.5}, \tag{A2}$$

where q_0 is the surface drift at the point of long-wave profile where the surface displacement $\zeta = 0$.

The relation between the long-wave phase speed C and the amplitude u_0 of long-wave orbital velocity is

$$\beta_s = \frac{u_0}{C}, \tag{A3}$$

where β_s is the long-wave slope and u_0 is the amplitude of the long-wave orbital velocity component in the alongwind direction.

Substituting (A1), (A2), and (A3) into (25), we have

$$\frac{q_{\max}}{u_0} = \frac{(1-\beta_s)}{\beta_s}\left\{1 - \left[1 - \frac{\alpha_1\alpha_2(2-\alpha_1\alpha_2)}{(1-\beta_s)^2}\right]^{1/2}\right\}, \tag{A4}$$

where $\alpha_1 = 0.877$, $\alpha_2 = 0.035$, $q_{\max}$ represents the maximum value of the surface drift at crest ($\theta = 0$). The right side of (A4) is called the proportional coefficient. The coefficient versus the long-wave slope is shown in Fig. A1. It is found empirically that this coefficient is approximately a constant with a mean value of about 0.15 in the range of slopes from 0.15 to 0.70 in the open ocean.

So, we have

$$q_{\max} = au_0, \tag{A5}$$

where a is a constant with a value of about 0.15 for the open ocean.

If we use

$$\bar{q} = \frac{3.5}{100} U_{19.5} \tag{A6}$$

to replace (A2), the relation (A5) can still be obtained. Here $\bar{q}$ represents the mean value of the surface drift at a period of long wave. Figures A2a and A2b are obtained from (25), (A1), (A3), and (A6). Figure A2a shows the long-wave slope versus the wind speed in the three different cases. The differences of the slopes are large, as shown by a solid line and two dashed lines. The corresponding drift at the crest, augmented by the long-wave orbital velocity, versus the long-wave orbital velocity are shown in Fig. A2b. It is found that the influence from long-wave slope is suppressed and the drift currents can be approximately expressed as a linear function of the long-wave orbital velocity. This means that (A5) is approximately correct when (A2) is replaced by (A6).

For the wind wave tunnel, the binding relation between the long-wave phase speed and the wind speed will be different. For example, a relationship obtained

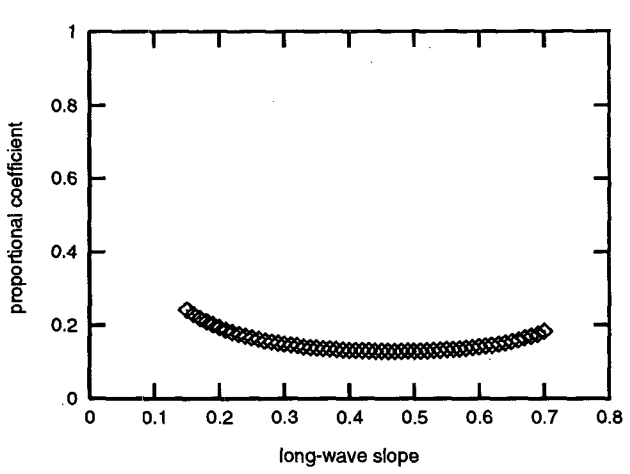

FIG. A1. The proportional coefficient, which is expressed by the right side of (A4), vs the long-wave slope.

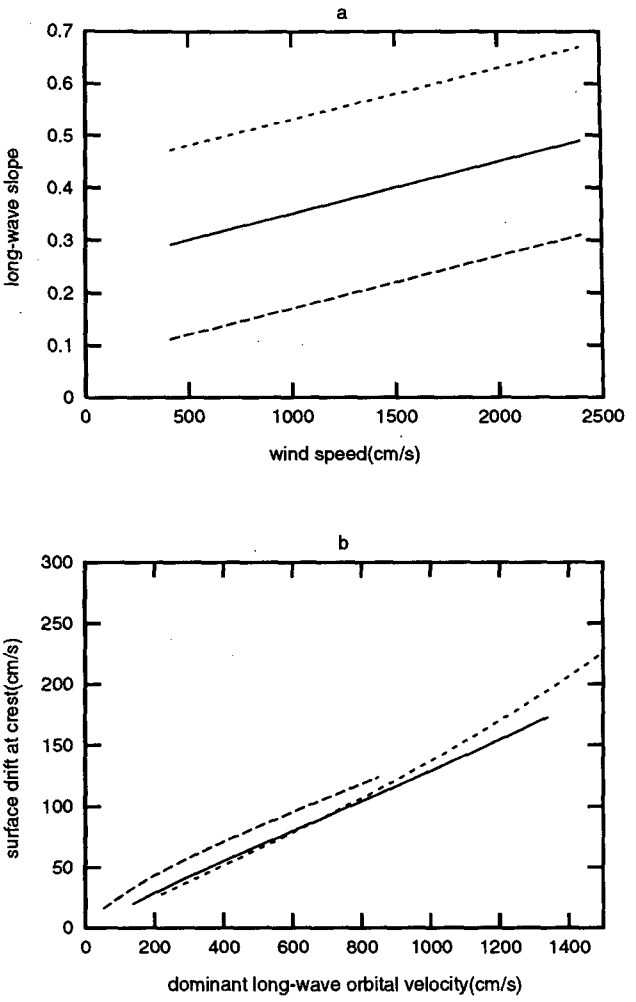

FIG. A2. The approximate linear relation between the surface drift at the crest and the long-wave orbital velocity in the condition of various slopes. It is found that the surface drift at crest, given by (25) and a few binding relations (A1), (A3), and (A6), is approximately proportional to the long-wave orbital velocity. (a) The long-wave slope versus the wind speed in the three different cases. (b) The surface drift at crest, augmented by long-wave orbital velocity, versus the long-wave orbital velocity in the three cases.

from the measurements by Jähne and Riemer (1990) is

$$C = (16 \text{ cm s}^{-1}\, U_{10})^{1/2}. \quad \text{(A7)}$$

The relationship between the mean drift and the mean wind speed is similar to that in the open ocean. The proportional coefficient measured by Wu (1968) is about $4/100$. Using (A7) to replace (A1), we found that 1) the surface drift at crest is still proportional to the long-wave orbital velocity as shown in (A5), but the proportional coefficient a obviously increases and 2) the long-wave slopes are small (less than 0.25), otherwise the long waves will break. When the background long waves break, (A4) cannot be used to derive the surface drift at crest. The influence from the long-wave breaking has not been included in this study.

APPENDIX B

The Probability Distribution of the Amplitude of Long-Wave Orbital Velocity in the Alongwind Direction

Based on the statistical theory of random functions first developed by Rice (1945), Longuet-Higgins (1975) derived the probability density of the wave amplitude.

Assuming that the sea surface is Gaussian and that the energy spectrum is sufficiently narrow, the probability density of the wave amplitude a (defined as half the crest-to-trough wave height) is given by the well-known Rayleigh distribution

$$f(\epsilon) = \epsilon e^{-\epsilon^2/2}, \quad \epsilon = \frac{a}{\mu_0^{1/2}}, \quad \text{(B1)}$$

where μ_0 is the zeroth moment of the energy spectrum. (In fact, μ_0 is also the mean-square wave amplitude.) To verify the distribution, some comparisons with observations have been given (Longuet-Higgins 1975; Chakrabarti and Cooley 1977). These comparisons indicated that there appears to be a reasonable fit. Especially, data with spectral width from 0.57 to 0.8 still fit the Rayleigh distribution very well (Chakrabarti and Cooley 1977).

Assuming that the long-wave orbital velocity component in the alongwind direction is Gaussian and that the corresponding energy spectrum is narrow, the probability density of the amplitude of long-wave orbital velocity component in the alongwind direction is given by the Rayleigh distribution

$$f(\eta) = \eta e^{-\eta^2/2}, \quad \eta = \frac{u_0}{\mu_0^{1/2}}, \quad \text{(B2)}$$

where μ_0 is the zeroth moment of the energy spectrum of long-wave orbital component in the alongwind direction, u_0 is the amplitude of long-wave orbital velocity component in the alongwind direction. The proof of Eq. (B2) is the same as that given by Longuet-Higgins (1975).

The assumption of narrow energy spectrum of the component in the alongwind direction can be accepted, especially in the condition of strong winds. The spectral width of energy spectrum of long-wave orbital velocity component in the crosswind direction is much larger than that in the alongwind direction. So, the Rayleigh distribution cannot used to describe the component in the crosswind direction.

From the Rayleigh distribution (B2) and the criterion (35), the probability of short-wave breaking can be derived as

$$\begin{aligned} P\left(\eta > \frac{\alpha_0 c}{\cos\phi\mu_0^{1/2}}\right) &= \int_{\frac{\alpha_0 c}{\cos\phi\mu_0^{1/2}}}^{\infty} \eta \exp\left(-\frac{\eta^2}{2}\right) d\eta \\ &= \exp\left(-\frac{\alpha_0^2 c^2}{2\cos^2\phi\mu_0}\right), \end{aligned} \quad \text{(B3)}$$

where ϕ is the angle between the short waves and the mean wind direction.

The zeroth moment of the energy spectrum of long-wave orbital velocity component in the alongwind direction can be described by

$$\mu_0 = \int_0^{\infty} \int_{-\pi/2}^{\pi/2} \Phi(\omega, \theta) \cos^2(\theta) d\theta d\omega, \quad \text{(B4)}$$

where $\Phi(\omega, \theta)$ is the directional spectrum of long-wave orbital velocity and θ is the angle between the long-wave orbital velocity and the mean wind direction.

A simple form of the directional spectrum is given by

$$\Phi(\omega, \theta) = \begin{cases} K\Phi(\omega)\cos^{2p}\theta & \text{for } |\theta| \leq \pi/2 \\ 0 & \text{otherwise,} \end{cases} \quad \text{(B5)}$$

where K and p are constants, $K\Phi(\omega)$ is the frequency spectrum of long-wave orbital velocity component in the alongwind direction, and $\cos^{2p}\theta$ is its directional spreading function.

Substituting (B5) into (B4), we obtain

$$\begin{aligned} \mu_0 &= \int_0^{\infty} \int_{-\pi/2}^{\pi/2} K\Phi(\omega)\cos^{2(p+1)}\theta d\theta d\omega \\ &= \frac{2p+1}{2(p+1)} \int_0^{\infty} \int_{-\pi/2}^{\pi/2} K\Phi(\omega)\cos^{2p}\theta d\theta d\omega \\ &= \frac{2p+1}{2(p+1)} \int_0^{\infty} \Psi(\omega) d\omega \\ &= \frac{2p+1}{2(p+1)} \int_0^{\infty} A^2(\omega)\omega^2 d\omega \propto m_0, \end{aligned} \quad \text{(B6)}$$

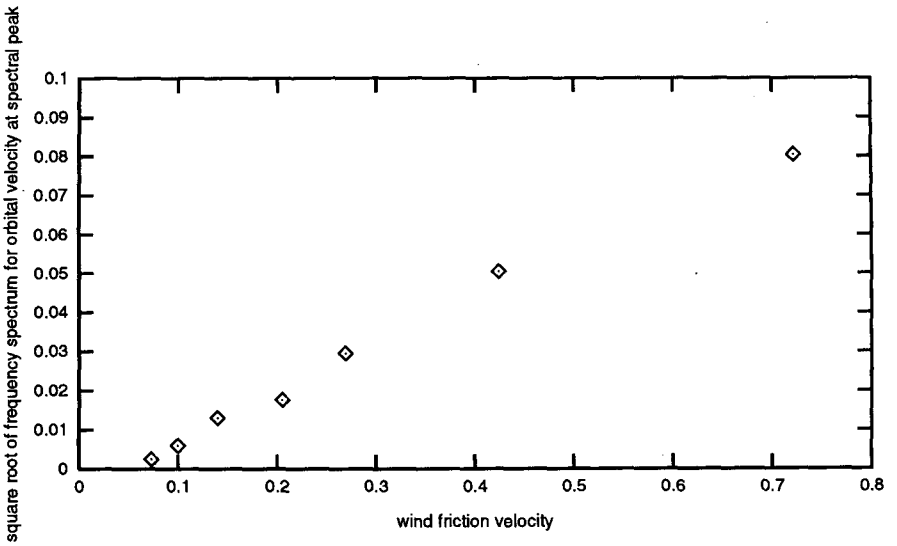

FIG. B1. Square root of the frequency spectrum of long-wave orbital velocity at spectral peak vs the wind friction velocity. The measurements from Jähne and Riemer (1990) show that $\Psi^{1/2}(\omega_p) \propto (u_* - 0.05\ \mathrm{m\ s^{-1}})$. The values of u_* are from their Table 2; the frequency spectrum of long-wave orbital velocity at spectral peak are calculated from $\Psi(\omega_p) = A^2(\omega_p)\omega_p^2 = B(f_p)k_p^{-4}\omega_p^2$, and the original data are from their Fig. 7.

where $\Psi(\omega)$ is the nondirectional frequency spectrum of long-wave orbital velocity, $A^2(\omega)$ is the nondirectional frequency spectrum of surface elevation, and m_0 is the zeroth moment of the nondirectional frequency spectrum of long-wave orbital velocity, which is defined by

$$m_0 = \int_0^\infty \Psi(\omega)d\omega = \int_0^\infty A^2(\omega)\omega^2 d\omega. \quad \text{(B7)}$$

From a nondirectional frequency spectrum of surface elevation, given by Pierson and Moscowitz (1964),

$$A^2(\omega) = \frac{\alpha g^2}{\omega^5}\exp\left[-\beta\left(\frac{g}{U_{19.5}\omega}\right)^4\right], \quad \text{(B8)}$$

with

$$\alpha = 8.10 \times 10^{-3}, \quad \beta = 0.74,$$

a relation between the zeroth moment m_0 and the wind speed $U_{19.5}$ at a height of 19.5 m over the ocean surface can be derived as

$$m_0 \propto U_{19.5}^2. \quad \text{(B9)}$$

Equation (B9) can be used in the case of the open ocean. For the narrow wind–wave tunnel, a different relation will be obtained. From the definition of m_0 [see (B7)], we have

$$m_0 = \int_0^\infty \Psi(\omega)d\omega \approx \int_{\omega_p-\Delta\omega}^{\omega_p+\Delta\omega} \Psi(\omega)d \approx \frac{1}{2}\Psi(\omega_p) \times [(\omega_p + \Delta\omega) - (\omega_p - \Delta\omega)] \propto \Psi(\omega_p), \quad \text{(B10)}$$

where ω_p is the angular frequency at the spectral peak. The above relationship is obtained approximately on the assumptions that the energy spectrum is sufficiently narrow and the spectrum width $2\Delta\omega$ is insensitive to the wind speed.

Figure B1 shows the square root of the nondirectional frequency spectrum of long-wave orbital velocity at spectral peak versus the wind friction velocity. The data in Fig. B1 are from the measurements by Jähne and Riemer (1990). An approximate relationship, found from Fig. B1, is

$$\Psi^{1/2}(\omega_p) \propto (u_* - 5\ \mathrm{cm\ s^{-1}}). \quad \text{(B11)}$$

Combined with (B10), we have

$$m_0 \propto (u_* - 5\ \mathrm{cm\ s^{-1}})^2. \quad \text{(B12)}$$

Equation (B9) indicates that the zeroth moment m_0 of nondirectional frequency spectrum of long-wave orbital velocity in the open ocean is proportional to the square of wind speed at a height over the ocean. Equation (B12) indicates that the zeroth moment m_0 in the wind–wave tunnel is proportional to the input wind stress. Actually, the value 5 cm s^{-1} in (B12) is present as a threshold wind friction velocity. Because the modulation from wave–drift interaction is significant only in the presence of strong winds, the influence from the threshold wind friction velocity in (B12) is negligible.

REFERENCES

Anderson, D., A. Hollingsworth, S. Uppala, and P. Woiceshyn, 1991: A study of the use of scatterometer data in the European Centre for Medium-Range Weather Forecasts operational analysis-

forecast model. 1: Quality assurance and validation. *J. Geophys. Res.*, **96,** 2619–2634.

——, ——, ——, and ——, 1991: A study of the use of scatterometer data in the European Center for Medium-Range Weather Forecasts operational analysis-forecast model. 2: Data impact. *J. Geophys. Res.*, **96,** 2635–2647.

Apel, J. R., 1987: *Principles of Ocean Physics.* Academic Press, 634 pp.

——, 1994: An improved model of the ocean surface wave vector spectrum and its effects on radar backscatter. *J. Geophys. Res.*, **99**(C8), 16 269–16 291.

Attema, E., Ed., 1992: ERS-1 geophysical validation. *Proc. Workshop at Penhors,* Bretagne, France, European Space Agency, 205 pp.

Banner, M. L., 1989: Wavenumber spectra of short gravity waves. *J. Fluid Mech.*, **198,** 321–344.

——, 1990: Equilibrium spectra of wind waves. *J. Phys. Oceanogr.*, **20,** 966–984.

——, 1991: On the directional behavior of the equilibrium wave number spectrum: Implication for the equilibrium frequency spectrum. *Directional Ocean Wave Spectra,* R. C. Beal, Ed., The Johns Hopkins University Press, 39–45.

——, and O. M. Phillips, 1974: On the incipient breaking of small-scale waves. *J. Fluid Mech.*, **4,** 647–656.

Barrick, D. E., 1968: Rough surface scattering based on the specular point theory. *IEEE Trans. Antennas Propag.*, **16,** 449–454.

Brown, G. S., 1978: Backscattering from a Gaussian-distributed perfectly conducting rough surface. *IEEE Trans. Antennas Propag.*, **26,** 472–482.

Chakrabarti, S. K., and R. P. Cooley, 1977: Statistical distribution of periods and heights of ocean waves. *J. Geophys. Res.*, **82**(9), 1363–1368.

Chang, P. C., E. J. Plate, and G. M. Hidy, 1971: Turbulent air flow over the dominant component of wind-generated water waves. *J. Fluid Mech.*, **47**(1), 183–208.

Cox, C. S., 1958: Measurements of slopes of high-frequency wind waves. *J. Mar. Res.*, **16,** 199–225.

Davidson, K. L., G. E. Schacher, G. W. Fairall, and J. D. Jarrell, 1981: Observational results pertaining to scatterometer interpretation. *Oceanography from Space,* J. F. R. Gower, Ed., Plenum Press, 597–606.

Dittmer, K. V., 1977: The hydrodynamic roughness of the sea surface at low wind speed. *"Meteor" Forschungsergeb., Reihe B,* **12,** S10–15.

Donelan, M. A., and W. J. Pierson, 1987: Radar scattering and equilibrium range in wind-generated waves with application to scatterometry. *J. Geophys. Res.*, **92,** 4971–5029.

——, J. Hamilton, and W. H. Hui, 1985: Directional spectra of wind generated waves. *Philos. Trans. Roy. Soc. London, Ser. A,* **315,** 509–562.

Durden, S. L., and J. F. Vesecky, 1985: A physical radar cross section model for a wind-driven sea with swell. *IEEE J. Oceanic Eng.*, **10,** 451–454.

Guignard, J. P., 1992: CMOD3 model description. ESA ESTEC ow, er tn esa jp 0016. Version 1.2.

Hasselmann, K., 1962: On the non-linear energy transfer in a gravity wave spectrum. Part 1. *J. Fluid Mech.*, **12,** 481–500.

——, 1963: On the non-linear energy transfer in a gravity wave spectrum. Part 2. *J. Fluid Mech.*, **15,** 273–281.

——, 1963b: On the non-linear energy transfer in a gravity wave spectrum. Part 3. *J. Fluid Mech.*, **15,** 385–398.

Hoffman, R. N., 1993: A preliminary study of the impact of the ERS 1 C band scatterometer wind data on the European Centre for Medium-Range Weather Forecasts global data assimilation system. *J. Geophys. Res.*, **98,** 10 233–10 244.

Hsiao, S. V., and O. H. Shemdin, 1983: Measurements of wind velocity and pressure with a water follower during MARSEN. *J. Geophys. Res.*, **88**(C14), 9841–9849.

Hwang, P. A., D. B. Trizna, and J. Wu, 1993: Spatial measurements of short wind waves using a scanning slope sensor. *Dyn. Atmos. Oceans,* **20,** 1–23.

Jähne, B., and K. S. Riemer, 1990: Two dimensional wave number spectra of small-scale water surface waves. *J. Geophys. Res.*, **95,** 11 531–11 546.

Jones, W. L., L. C. Schroeder, and J. L. Mitchell, 1977: Aircraft measurements of the microwave scattering signature of the ocean. *IEEE Trans. Antennas Propag.*, **25,** 52–61.

Kahma, K. K., and M. A. Donelan, 1988: A laboratory study of the minimum wind speed for wind wave generation. *J. Fluid Mech.*, **192,** 339–364.

Kawai, S., K. Okuda, and Y. Toba, 1977: Field data support of three-seconds power law and $gu_*\sigma^{-4}$ spectral form for growing wind waves. *J. Oceanogr. Soc. Japan,* **33,** 137–150.

Keller, W. C., W. J. Plant, and D. E. Weissman, 1985: The dependence of X band microwave sea return on atmospheric stability and sea state. *J. Geophys. Res.*, **90,** 1019–1029.

Kitaigorodskii, K. A., 1983: On the theory of the equilibrium range in the spectrum of wind-generated gravity waves. *J. Phys. Oceanogr.*, **13,** 816–827.

Klein, L. A., and C. T. Swift, 1977: An improved model for the dielectric constant of sea water at microwave frequencies. *IEEE Trans. Antennas Propag.*, **25,** 104–111.

Klinke, J., and B. Jähne, 1992: 2D wave number spectra of short wind waves—Results from wind wave facilities and extrapolation to the ocean. *Optics of the Air–Sea Interface: Theory and Measurements, Proc. SPIE Int. Soc. Opt. Eng.*, **1749,** 1–13.

Komen, G. J., and W. A. Oost, Ed., 1989: *Radar Scattering from Modulated Wind Waves.* Kluwer, 273 pp.

Lamb, H., 1932: *Hydrodynamics.* 6th ed. Cambridge University Press, 738 pp.

Large, W. G., and S. Pond, 1981: Open ocean momentum flux measurements in moderate to strong winds. *J. Phys. Oceanogr.*, **11,** 324–326.

Larson, T. R., and J. W. Wright, 1975: Wind-generated gravity-capillary waves: Laboratory measurements of temporal growth rates using microwave backscatter. *J. Fluid Mech.*, **70,** 417–436.

Liu, Y., and W. J. Pierson, 1994: Comparisons of scatterometer models for the AMI on ERS-1: The possibility of systematic azimuth angle biases of wind speed and direction. *IEEE Trans. Geosci. Remote Sens.*, **32,** 626–635.

Long, A. E., 1986: Towards a C-band radar sea echo model for the ERS-1 scatterometer. *Proc. Conf. on Spectral Signatures,* Les Arc, France, ESA SP-247, 29–34.

Longuet-Higgins, M. S., 1963: The generation of capillary gravity waves by steep gravity waves. *J. Fluid Mech.*, **16,** 138–159.

——, 1969: On wave breaking and the equilibrium spectrum of wind generated waves. *Proc. Roy. Soc. London, Ser. A,* **311,** 371–389.

——, 1975: On the joint distribution of the periods and amplitudes of sea waves. *J. Geophys. Res.*, **80,** 2688–2694.

——, 1987: The propagation of short surface waves on longer gravity waves. *J. Fluid Mech.*, **177,** 293–306.

McGoldrick, L. F., 1965: Resonant interactions among capillary-gravity waves. *J. Fluid Mech.*, **21,** 305–332.

Miles, J. W., 1957: On the generation of surface waves by shear flow. *J. Fluid Mech.*, **3,** 185–204.

——, 1959: On the generation of surface waves by shear flow. Part 2: *J. Fluid Mech.*, **6,** 568–582.

Neumann, G., 1953: On ocean wave spectra and a new method of forecasting wind-generated sea. Beach Erosion Board, U.S. Army Corps of Engineers, Tech. Memo. 43, 42 pp.

Phillips, O. M., 1977: *The Dynamics of the Upper Ocean.* 2d ed. Cambridge University Press, 336 pp.

——, 1985: Spectral and statistical properties of the equilibrium range in the wind-generated gravity waves. *J. Fluid Mech.*, **156,** 505–531.

——, 1988: Radar returns from the sea surface—Bragg scattering and breaking waves. *J. Phys. Oceanogr.*, **18,** 1065–1074.

——, and M. L. Banner, 1974: Wave breaking in the presence of wind drift and swell. *J. Fluid Mech.*, **66,** 625–640.

Pierson, W. J., and L. Moscowitz, 1964: A proposed spectral form for fully developed wind seas based on the similarity theory of S. A. Kitaigorodskii. *J. Geophys. Res.*, **69**(24), 5181–5190.

——, W. B. Sylvester, and R. E. Salfi, 1981: Synoptic scale wind field properties from the SEASAT SASS. NASA Contractor Rep. 3810, Grant NAGW-266, 216 pp.

Plant, W. J., 1982: A relationship between wind stress and wave slope. *J. Geophys. Res.*, **87**, 1961–1967.

——, 1986: A two-scale model of short wind-generated waves and scatterometry. *J. Geophys. Res.*, **91**, 10 735–10 749.

Quilfen, Y., 1993: ERS 1 off-line wind scatterometer products. Version 1.0, IFREMER-BP 70-29280 Plouzaé-France,

Reynolds, W. C., and A. K. M. F. Hussain, 1972: The mechanics of an organized wave in turbulent shear flow. Part 3: Theoretical models and comparisons with experiments. *J. Fluid Mech.*, **54**(2), 263–288.

Rice, S. O., 1945: Mathematical analysis of random noise. *Bell System Tech. J.*, **24**, 46–156.

Schanda, E., Ed., 1976: *Remote Sensing for Environmental Sciences.* Springer-Verlag, 367 pp.

Shemdin, O. H., H. M. Tran, and S. C. Wu, 1988: Directional measurement of short ocean waves with stereophotography. *J. Geophys. Res.*, **93**, 13 891–13 901.

Shyu, J. H., and O. M. Phillips, 1990: The blockage of gravity and capillary waves by longer waves and currents. *J. Fluid Mech.*, **217**, 115–141.

Smith, J., 1986: Short surface waves with growth and dissipation. *J. Geophys. Res.*, **91**, 2616–2632.

——, 1990: Modulation of short wind waves by long waves. *Surface Waves and Fluxes,* Vol. 1, G. L. Geernaert and W. L. Plant, Eds., Kluwer Academic Publishers, 247–284.

Snyder, R. L., F. W. Dobson, J. A. Elliott, and R. B. Long, 1981: Array measurements of atmospheric pressure fluctuation above surface gravity waves. *J. Fluid Mech.*, **102**, 1–59.

Stewart, R. W., 1974: The air–sea momentum exchange. *Bound.-Layer Meteor.*, **6**, 151–167.

——, 1985: *Methods of Satellite Oceanography.* University of California Press, 360 pp.

Stoffelen, A., and D. L. T. Anderson, 1992: ERS-1 scatterometer calibration and validation activities at ECMWF: A. The quality and characteristics of the radar backscatter measurements. *Proc. European 'Int. Space Year' Conf.,* Munich, Germany, European Space Agency, 83–88.

——, ——, and P. M. Woiceshyn, 1992: ERS-1 scatterometer calibration and validation activities at ECMWF: B. From radar backscatter characteristics to wind vector solutions. *Proc. European 'Int. Space Year' Conf.,* Munich, Germany, European Space Agency, 89–94.

Takeuchi, K., E. Leavitt, and S. P. Chao, 1977: Effects of water waves on the structure of turbulent shear flow. *J. Fluid Mech.*, **80**(3), 535–559.

Thornton, E. B., 1977: Rederivation of the saturation range in the frequency spectrum of wind-generated gravity waves. *J. Phys. Oceanogr.*, **7**, 137–140.

Toba, Y., 1973: Local balance in the air–sea boundary processes. Part 3: On the spectrum of wind waves. *J. Oceanogr. Soc. Japan,* **29**, 209–220.

Townsend, A. A., 1972: Flow in a deep turbulent boundary layer over a surface distorted by water waves. *J. Fluid Mech.*, **55**, 719–735.

Valenzuela, G. R., 1976: The growth of gravity-capillary waves in a coupled shear flow. *J. Fluid Mech.*, **76**, 229–250.

——, 1978: Theories for the interaction of electromagnetic and ocean wave—A review. *Bound.-Layer Meteor.*, **13**, 61–85.

Van Gastel, K., P. A. E. M. Janssen, and G. J. Komen, 1985: On phase velocity and growth rate of wind-induced gravity–capillary waves. *J. Fluid Mech.*, **161**, 199–216.

Wen, S., and Z. Yu, 1984: *Wave Theory and Calculation Principle* (in Chinese). Science Press, 662 pp.

Woiceshyn, P., T. W. Yu, and W. Gemmill, 1993: Use of ERS-1 scatterometer data to derive ocean surface winds at NMC. Preprints, *13th Conf. on Weather Analysis and Forecasting Including Symp. on Flash Floods,* Vienna, VA, Amer. Meteor. Soc., 239–240.

Wright, J. W., 1968: A new model for sea clutter. *IEEE Trans. Antennas Propag.*, **16**, 217–223.

Wu, J., 1968: Laboratory studies of wind–wave interactions. *J. Fluid Mech.*, **34**, 91–111.

——, 1994: Altimeter wind and wind-stress algorithms—Further refinement and validation. *J. Atmos. Oceanic Technol.*, **11**, 210–215.

Zhao, M., 1994: Experimental study of fine structures of wind-disturbed water surface. Ph.D dissertation, University of Delaware, 244 pp.